

1 **SUBSTRATE ENTRAINMENT, DEPOSITIONAL RELIEF, AND SEDIMENT**
2 **CAPTURE: IMPACT OF A SUBMARINE LANDSLIDE ON FLOW PROCESS AND**
3 **SEDIMENT SUPPLY**

4

5 **Authors:**

6 *Martínez-Doñate, A.¹, Privat, A. M-L. J.², Hodgson, D.M.², Jackson, C.A-L.¹, Kane, I.A.¹,*
7 *Spychala, Y. T. ³, Duller, R.A.⁴, Stevenson, C.⁴, Keavney, E. ², Schwarz, E.⁵, Flint, S.S.¹*

8 • *School of Earth and Environmental Sciences, University of Manchester, Manchester M13*
9 *9PL, UK.*

10 • *School of Earth and Environment, University of Leeds, Leeds LS29JT, UK.*

11 • *Institute for Geology, Leibniz University Hannover, Callinstraße 30, Hannover 30167,*
12 *Germany*

13 • *Department on Earth, Ocean, and Ecological Sciences, University of Liverpool, 4*
14 *Brownlow Street, Liverpool L69 3GP, UK*

15 • *Centro de Investigaciones Geológicas (CIG), La Plata, Provincia de Buenos Aires,*
16 *Argentina*

17

18 **Corresponding author:** ander.martinez-donate@manchester.ac.uk

19

20 **ABSTRACT:**

21 Submarine landslides can generate complicated patterns of seafloor relief that influence
22 subsequent flow behaviour and sediment dispersal patterns. In subsurface studies, the term
23 mass transport deposits (MTDs) is commonly used and covers a range of processes and
24 resultant deposits. While the large-scale morphology of submarine landslide deposits can be
25 resolved in seismic data, the nature of their upper surface and its impact on both facies

26 distributions and stratal architecture of overlying deposits is rarely resolvable. However, field-
27 based studies often allow a more detailed characterisation of the deposit. The early post-rift
28 Middle Jurassic deep-water succession of the Los Molles Formation is exceptionally well-
29 exposed along dip-orientated WSW-ENE outcrop belt in the Chacay Melehue depocentre,
30 Neuquén Basin, Argentina. We correlate 27 sedimentary logs constrained by marker beds to
31 document the sedimentology and architecture of a >47 m thick and at least 9.6 km long debrite,
32 which comprises two different types of megaclasts. The debrite overlies ramps and steps,
33 indicating erosion and substrate entrainment. Two distinct sandstone-dominated units overlie
34 the debrite. The lower sandstone unit is characterised by: i) abrupt thickness changes, wedging
35 and progressive rotation of laminae in sandstone beds associated with growth strata; and ii)
36 detached sandstone load balls within the underlying debrite. The combination of these features
37 suggests syn-sedimentary foundering processes due to density instabilities at the top of the
38 fluid-saturated mud-rich debrite. The debrite relief controlled the spatial distribution of
39 foundered sandstones. The upper sandstone unit is characterised by thin-bedded deposits,
40 locally overlain by medium- to thick-bedded lobe axis/off-axis deposits. The thin-beds show
41 local thinning and onlapping onto the debrite, where it develops its highest relief. Facies
42 distributions and stacking patterns record the progradation of submarine lobes and their
43 complex interaction with long-lived debrite-related topography. The emplacement of a
44 kilometre-scale debrite in an otherwise mud-rich basinal setting and accumulation of overlying
45 sand-rich deposits suggests a genetic link between the mass-wasting event and transient coarse
46 clastic sediment supply to an otherwise sand-starved part of the basin. Therefore, submarine
47 landslides demonstrably impact the routing and behaviour of subsequent sediment gravity
48 flows, which must be considered when predicting facies distributions and palaeoenvironments
49 above MTDs in subsurface datasets.

50 **Keywords:** Submarine Landslide, Submarine lobe, Foundering, Dynamic topography, Relief,
51 Confinement, Neuquén Basin.

52

53 **INTRODUCTION**

54 Submarine landslide deposits, olistostromes (Flores, 1955), or Mass Transport Deposits
55 (MTDs) (Nardin *et al.*, 1979), are sedimentary bodies that have been translated downslope from
56 high to low gradient slopes as a result of mass failure and gravitational processes (Hampton *et*
57 *al.*, 1995; Moscardelli & Wood, 2008; Ogata *et al.*, 2012; Festa *et al.*, 2016; Kneller *et al.*,
58 2016). The typically cohesive nature of the flows enables the transportation of large clasts (>
59 4.1m; herein named megaclasts, sensu Blair & McPherson, 1999) (Labaume *et al.*, 1987;
60 Payros *et al.*, 1999; McGilvery & Cook, 2003; Lee *et al.*, 2004; Jackson, 2011; Ogata *et al.*,
61 2012; Hodgson *et al.*, 2019; Nwoko *et al.*, 2020a). Megaclasts within MTDs are sourced either
62 from headwall areas or entrained from the substrate (Festa *et al.*, 2016; Ogata *et al.*, 2019).
63 These features, accompanied by syn- and post-depositional faulting (Dykstra, 2005; Dykstra *et*
64 *al.*, 2011), generate the topographically irregular upper surfaces of MTDs (Moscardelli *et al.*,
65 2006; Bull *et al.*, 2009).

66 Deep-water sediment gravity flows interact with the rugose topography of MTDs, which
67 influences flow behaviour, deceleration and steadiness (Lowe & Guy, 2000; Armitage *et al.*,
68 2009; Jackson & Johnson, 2009; Fairweather, 2014; Ortiz-Karpf *et al.*, 2015, 2017; Steventon
69 *et al.*, 2021), and therefore dispersal patterns and depositional architecture (Kneller *et al.*,
70 2016). MTD surface relief has been shown to affect facies distribution and associated
71 sedimentary architecture; this has been reported from both outcrop (Pickering & Corregidor,
72 2005; Armitage *et al.*, 2009; Dykstra *et al.*, 2011; Fallgatter *et al.*, 2017; Brooks *et al.*, 2018;
73 Valdez *et al.*, 2019) and subsurface studies (Ortiz-Karpf *et al.*, 2017; Nwoko *et al.*, 2020b).

74 However, MTDs may continue to deform after initial emplacement through creeping processes
75 (e.g. Butler & McCaffrey, 2010) or secondary mass movements (Sobiesiak *et al.*, 2016).
76 Furthermore, the high water content within newly deposited MTDs promotes active dewatering
77 at their upper surface (Mulder & Alexander, 2001; Talling *et al.*, 2012; Browne *et al.*, 2020)
78 associated with local instabilities and movement (Iverson, 1997; Major & Iverson, 1999; Van
79 der Merwe *et al.*, 2009). Fluids can also generate overpressure along with the interface between
80 MTDs and its sediment cover, exploiting pathways created by internal MTD deformation
81 (Ogata *et al.*, 2012; Migeon *et al.*, 2014; Praeg *et al.*, 2014). Therefore, the interaction between
82 the initial topographic relief of MTDs, dewatering processes, post-depositional deformation
83 and subsequent sediment gravity flows (and their deposits) is highly dynamic and inherently
84 complex (e.g. Alves, 2015). A better understanding of sedimentary processes above MTDs can
85 help subsurface predictions of facies distributions, which might have been overlooked due to
86 variable seismic resolution and core coverage. Therefore, detailed field-based studies can help
87 to bridge the resolution gap.

88 Here, we aim to understand an exceptionally well-exposed debrite and overlying sand-rich
89 strata in the Bathonian Los Molles Formation, which were physically correlated over 9.6 km
90 along a depositional dip transect in the Chacay Melehue depocenter (Neuquén Basin,
91 Argentina). The objectives of this study are to i) document the anatomy and stratigraphic
92 architecture of the debrite, ii) investigate the impact of the dynamic upper relief on the
93 overlying heterolithic and sand-rich strata, and iii) discuss the role that mass-wasting processes
94 may have played as a trigger for subsequent sand-rich sediment supply.

95

96 **GEOLOGICAL SETTING**

97 The Neuquén Basin is located in central-western Argentina and central-eastern Chile, covering
98 an area of 160,000 km² (Fig. 1A). The basin is bounded to the north-east by the Sierra Pintada,

99 to the south by the North Patagonian Massif, and since the Early Jurassic, by the early Andean
100 magmatic arc to the west (Legarreta & Gulisano, 1989; Suárez & de la Cruz, 1997; Franzese
101 & Spalletti, 2001; Howell *et al.*, 2005). The Neuquén Basin contains a >6 km-thick sedimentary
102 succession that spans the Mesozoic to the Late Cenozoic and records several unconformities
103 related to tectonic phases (Vergani *et al.*, 1995; Legarreta & Uliana, 1996; Howell *et al.*, 2005).
104 Three key tectonic phases are recognised (Vergani *et al.*, 1995; Franzese & Spalletti, 2001;
105 Franzese *et al.*, 2003): i) Triassic-to-Early Jurassic rifting and the onset of subsidence; ii) Early
106 Jurassic-to-Early Cretaceous post-rift thermal subsidence associated with the development of
107 the Andean magmatic arc and back-arc basin; and iii) Late Cretaceous-to-Early Cenozoic
108 Andean compression and foreland basin development. In the western sector of the Central
109 Neuquén Basin, the deep- to shallow-marine deposits of the early post-rift Cuyo Group (Lower-
110 to-Middle Jurassic) (Gulisano *et al.*, 1984) unconformably overlie the continental syn-rift
111 volcano-sedimentary deposits of the Precuyano Group (Gulisano *et al.*, 1984; Gulisano &
112 Gutiérrez Pleimling, 1995; Legarreta & Uliana, 1996; Pángaro *et al.*, 2009; Leanza *et al.*, 2013)
113 or the Palaeozoic basement of the Choiyoi Group (Llambías *et al.*, 2003, 2007) (Fig. 2A).
114 Our investigation focuses on the Early Bathonian stratigraphy of the Upper Los Molles
115 Formation, which forms a ~70 m thick interval characterised by ammonite-rich black shales
116 and heterolithic successions comprising tuff layers with an intervening MTD and sandstone
117 deposits (Fig. 1B).

118

119 **Study area - Chacay Melehue depocentre**

120 The succession in the Chacay Melehue area was deposited in a half-graben (~20 km long)
121 (Maceda & Figueroa, 1995; Llambías *et al.*, 2007; Leanza *et al.*, 2013) that occupied the
122 western and deepest part of a broader early post-rift depocentre in the Central Neuquén Basin
123 (~65 km long) (Maceda & Figueroa, 1995; Veiga *et al.*, 2013). The half-graben shows a strong

124 asymmetry due to a steep western margin characterised by the development of the early Andean
125 magmatic arc and location of a major syn-rift fault (Manceda & Figueroa, 1995; Suárez & de
126 la Cruz, 1997; Vicente, 2005), which contrasts with the stable and gently dipping eastern
127 cratonic margin (Spalletti *et al.*, 2012; Veiga *et al.*, 2013). Deposition of the Los Molles
128 Formation took place during a period of thermal subsidence and regional transgression across
129 complex inherited rift topography, which promoted the reduction of sediment supply and sand
130 starvation in this part of the basin (Spalletti *et al.*, 2012; Veiga *et al.*, 2013). The proximity to
131 the volcanic arc (~30 km to the west), the abundant volcanoclastic deposits (Zöllner & Amos,
132 1973; Rosenfeld & Volldaeimer, 1980; Gulisano & Gutiérrez Pleimling, 1995; Suárez & de la
133 Cruz, 1997; Vicente, 2005; Llambías *et al.*, 2007), and palaeocurrent measurements in
134 sandstones indicating southeastwards trend reveals that sediment supply feeding the Chacay
135 Melehue area during the post-rift was sourced from the western magmatic arc (Gulisano *et al.*,
136 1984; Vicente, 2005). The deep-marine deposits of Los Molles Formation (Weaver, 1931)
137 overlie shallow-marine tuffaceous clastic deposits (La Primavera Formation, Suárez & de la
138 Cruz, 1997; Llambías & Leanza, 2005) and carbonate deposits of the Chachil Formation
139 (Pliensbachian to Early Toarcian, Weaver, 1942; Kamo & Riccardi, 2009; Leanza *et al.*, 2013;
140 Riccardi & Kamo, 2014), deposited with the first marine incursion in the basin (Gulisano &
141 Gutiérrez Pleimling, 1995; Leanza *et al.*, 2013) (Fig. 2A). Chronostratigraphic studies based
142 on ammonite biostratigraphy (Gulisano & Gutiérrez Pleimling, 1995; Riccardi, 2008) and U-
143 Pb radiometric dating (Kamo & Riccardi, 2009; Leanza *et al.*, 2013; Riccardi & Kamo, 2014),
144 place the Los Molles Formation in the Chacay Melehue region as Early Toarcian-to-Early
145 Callovian in age (Gulisano & Gutiérrez Pleimling, 1995) (Fig. 2C). The succession of the Los
146 Molles Formation in the Chacay Melehue depocentre is 850 m thick (Fig. 2B). A 55 m thick
147 sandstone-prone interval in the lower succession represents an Aalenian turbidite system
148 (interval II of Gulisano & Gutiérrez Pleimling, 1995). The overlying Bathonian section of the

149 Los Molles Formation (up to 200 m thick) (Fig. 2B) is mainly represented by mudstone and
150 heterolithic successions, including a 70 m thick interval (study interval; Fig 2C) of deformed
151 sand- and mud-rich deposits (interval IV of Gulisano & Gutiérrez Pleimling, 1995). The
152 overlying Lower Callovian strata of the Los Molles Formation is characterised by a 300 m
153 thick interval of thin-bedded mudstone. It is overlain by either the fluvial Lotena Formation
154 (Gulisano & Gutiérrez Pleimling, 1995; Veiga *et al.*, 2011) or evaporites (Tábanos Formation;
155 Fig. 2D), which record a period of basin desiccation (Legarreta, 1991; Gulisano & Gutiérrez
156 Pleimling, 1995; Legarreta & Uliana, 1996).

157

158 **METHODOLOGY**

159 The sedimentology and stratigraphic architecture of a 70 m thick interval (Figs. 2C and 3)
160 within the Upper Los Molles Formation were investigated along a 9.6 km long and WSW-ENE
161 orientated outcrop belt (Figs. 1B and 1C). The succession dips 10-20° to the SE, with minimal
162 structural overprint from the later tectonic inversion. Twenty-seven (27) sedimentary logs were
163 measured at 1:25 to 1:40 scale along this transect (CML-0 to CML-27 from SW to NE) to
164 document the broad depositional architecture of 4 different units (Unit 1, 2, 3, 4A and B) (Fig.
165 1C). Ten detailed logs were measured at a 1:2 scale at specific locations to document fine-scale
166 thickness and facies changes. Four marker beds were used to build a robust physical correlation
167 between sedimentary logs (Figs. 2 and 3). The marker beds are i) Datum A, or the 'Burro'
168 marker bed, a light-grey indurated graded siltstone at the base of the study interval (Figs. 2A,
169 3 and 4A); ii) a gravelly thin-bed (Fig. 4F) and iii) a tuff layer (Fig. 4G), both within one of the
170 studied units (Unit 4A); and iv) Datum B, a tuff layer overlying the study interval (100-150 m
171 above) across the study area (Figs. 2D and 3). Uncrewed Aerial Vehicle (UAV)
172 photogrammetry (Figs. 2D and 5) was used in conjunction with standard field techniques, such
173 as mapping and logging, to capture the micro- and macro-scale features of the investigated

174 stratigraphic units. Fifty-eight (58) palaeocurrent measurements were collected, consisting of
175 ripples, cross-bedding, flame structure and convolute lamination vergence from bed tops of
176 sandstones, and plotted in rose diagrams.

177

178 **RESULTS: SUBDIVISION AND CHARACTERISATION OF SEDIMENTARY UNITS**

179 **1-4**

180 The study interval is subdivided informally into four different units (Fig. 2C), based on their
181 distinctive facies (Table 1) and stratal relationships.

182 **Unit 1**

183 Description: Unit 1 is 5.5-28 m thick and contains the Burro marker bed (Datum A) (Fig. 2C),
184 a light-grey indurated graded siltstone that is sharply overlain by light-grey fine-grained,
185 planar-parallel laminated sandstone (Fig. 4A). This unit is truncated by the basal surface of
186 Unit 2 and is thinnest in the central sector of the exposure (see sections CML-9 to CML-16
187 Fig. 3). Unit 1 comprises a heterolithic succession of planar-parallel laminated mudstones (F1)
188 and thin-bedded (<0.1 m thick) normally-graded, well-sorted siltstones (F2) to very fine-
189 grained sandstones (F3), and occasional medium-bedded structureless sandstones (F5) (Figs.
190 4A and 4C). When traced from west to east, the thin-bedded sandstones show subtle lateral
191 fining and thinning, transitioning from heterolithic succession to mudstone-prone succession.
192 Unit 1 is rich in ammonites, belemnite rostrums and bivalves, as well as calcareous concretions
193 (Damborenea, 1990; Gulisano & Gutiérrez Pleimling, 1995; Riccardi *et al.*, 2011).

194 The central and eastern sectors contain a discrete stratigraphic interval that exhibits deformed
195 bedding (Fig. 4B). This interval is thickest (at least 10 m; Fig. 3) in the central sector, where,
196 internally, it exhibits an array of imbricated decametre-scale east-verging thrusts (offset < 2 m)
197 and associated drag folds. The thrusts originate from a bed parallel surface, leaving the
198 underlying bedding undeformed (Fig. 4B). In the eastern sector, a thin (~5 m thick) interval of

199 intense deformation is characterised by open folds and minor thrusts (offset < 1 m) (Fig 4B).
200 Unit 1 stratigraphy in the western sector lacks any deformation.

201

202 Interpretation: The laminated mudstones, graded siltstones and thin sandstone beds are
203 interpreted as deposits of low-density turbidity currents (Allen, 1982; Trabucho-Alexandre *et al.*,
204 *al.*, 2012; Könitzer *et al.*, 2014), whereas the medium-bedded sandstones represent the deposits
205 of medium- to high-density turbidity current (Talling *et al.*, 2012). The laterally extensive
206 character, mudstone dominance, and overall eastward (downdip) fining and thinning trend of
207 thin-bedded sandstones of Unit 1 suggest deposition from low-energy sediment gravity flows
208 in distal areas (e.g. Mutti, 1977), with possible distal lobe fringe deposits (Boulestex *et al.*,
209 2020). The discrete intervals of deformed bedding found in the upper parts of Unit 1 represent
210 a post-depositional sheared zone linked to the overlying Unit 2.

211 **Unit 2**

212 Description: Unit 2 has an unconformable basal contact that truncates Unit 1 in the central
213 sector (Fig. 3). The relief of the basal contact is characterised by down- and up-stepping
214 segments (ramps, >2°) linked by bedding-parallel segments (flats). The average thickness of
215 Unit 2 is 20-30 m but can locally reach up to > 47m in the central sector and abruptly thins to
216 <8 m towards the eastern and western sectors (Fig. 3). This change in thickness coincides with
217 deeper erosion on the basal surface.

218 Unit 2 is characterised by a matrix-supported medium-grained muddy sandstone to sandy
219 mudstone and is very poorly sorted throughout, ungraded, and with a chaotic distribution of
220 outsized clasts(F14; Fig 5). Clasts range in character and size from granular quartz grains and
221 rounded volcanic epiclasts to much larger megaclasts (>4.1 - 140 m long) (Hodgson *et al.*,
222 2019) of either conglomeratic or heterolithic lithology (Figs. 2C, 2D, 4F and 5). The chaotic
223 distribution of polymictic clast encased into a muddy sand matrix is responsible for the block-

224 in-matrix fabric (e.g. Ogata *et al.*, 2012). Typically, conglomeratic megaclasts are rounded,
225 elongated and weakly deformed (Figs. 2D, 4F and 4G) and are clast-supported, with well-
226 rounded to sub-angular clasts (0.03-1 m diameter) and fragments of thick-shelled bivalves
227 (oysters; Fig. 4D). These oyster-bearing conglomeratic megaclasts are preferentially located
228 near the base of Unit 2 (Figs. 2C, 2D and 3B). In contrast, heterolithic megaclasts are angular
229 and characterised by internally folded packages of planar laminated and normally graded thin-
230 bedded material (Figs. 2C and 5) and preferentially distributed toward the top of Unit 2 (Figs.
231 3 and 5). This heterogeneity promotes a homogeneous matrix-rich texture in the middle
232 division.

233 Apart from the irregular basal contact of Unit 2, thickness changes within the unit are strongly
234 controlled by the rugose upper surface. Kilometre-scale wavelength (1-3 km) and metre-scale
235 amplitudes (0.5-8 m) are responsible for a complex supra debrite topography.

236

237 Interpretation: The sedimentary characteristics of this unit, such as the chaotic distribution of
238 (mega)clast floating onto a muddy sandstone to sandy mudstone matrix, suggest near-
239 instantaneous deposition from a flow with high yield strength and buoyant support that could
240 transport clasts up to 140 m long (Stow & Johansson, 2000; Mulder & Alexander, 2001). Using
241 Datum A, the debrite formed a long-wavelength mounded top (Fig. 3), attributed to the parental
242 flow's cohesive nature and en-masse freezing. We interpret Unit 2 as a cohesive debris flow
243 deposit (Talling *et al.*, 2012). The ramp and flat geometry at the base of Unit 2 indicate the
244 debris flow's erosive nature (e.g. Lucente & Pini, 2003). The similarity in composition between
245 the heterolithic megaclasts and underlying Unit 1 suggests entrainment of deep-marine
246 substrate blocks due to the shear stress exerted by the overriding debris flow (Van der Merwe
247 *et al.*, 2009; Watt *et al.*, 2012; Ogata *et al.*, 2014a; Hodgson *et al.*, 2019). In contrast, the sand
248 content in the matrix and the oyster-bearing conglomerate megaclasts suggest a shallow marine

249 origin of the mass failure (e.g. Ogata *et al.*, 2012). Alternatively, the megaclast bearing shells
250 could come from the remobilization of older slope strata, including shallow-marine deposits
251 (La Primavera Fm; Suárez & de la Cruz, 1997; Llambías & Leanza, 2005). The two distinct
252 megaclast sources suggest long-distance transport of clasts and flow bulking through local
253 substrate entrainment (e.g. Sobiesiak *et al.*, 2016).

254

255 **Unit 3**

256 Description: Unit 3 (0-4 m thick) is composed of thick sandstone beds (0.5-2 m) with sharp,
257 irregular concave-up bases and abrupt pinchout terminations, which result in a disconnected
258 distribution of packages of wedge-shaped sandstone bodies (Fig. 6) (see architecture section).

259 Unit 3 is only present where Unit 2 is relatively thin (in the eastern-central and western sectors)
260 and is absent in the central region where Unit 2 shows its maximum thickness (Fig. 3). Where
261 Unit 3 is absent, Unit 4 overlies Unit 2 (Fig. 3). Unit 3 comprises bed types characterised by
262 two main amalgamated divisions (lower and upper divisions) with some grain size breaks
263 lacking any mudstone- and siltstone-rich bounding intervals (Figs. 6A and 7). The basal
264 interface of these sandstone bodies shows centimetre-scale undulations characterised by
265 abundant load casts, semi-detached ball structures, and mudstone intrusions (diapirs and
266 injectites) originating from Unit 2 (Fig. 6G).

267 Two different types of thick-bedded amalgamated sandstone facies dominate the lower
268 division, which varies along the transect. Grain-size breaks define amalgamation surfaces
269 within sandstones. In the western sector, and more rarely in the eastern sector, the lower
270 divisions are characterised by thick-bedded (0.5-2 m thick), structureless, weakly normally-
271 graded, moderately- to poorly-sorted sandstones (F12). At bed bases, these sandstones
272 comprise well-rounded (0.1-1 m diameter) mudstone clasts of low-sphericity and diffuse
273 boundaries (mudstone clast type A), which show a coarse tail grading (Figs. 6A and 6G).

274 Locally, in the eastern sector, lower divisions of these sandstone bodies comprise thick-bedded,
275 structureless, very poorly-sorted, more argillaceous sandstones with abundant mudstone clasts
276 (0.1 - 1 m diameter) with very diffuse boundaries (mudstone clast type A), which are ungraded
277 and randomly orientated (F13) throughout the encasing matrix (Fig. 5F).

278 The lower division of Unit 3 sandstone bodies are overlain by an upper division (up to 2 m
279 thick), which comprises coarse to very fine-grained, normally graded, moderately- to poorly-
280 sorted sandstones (0.5-1.7 m) (Fig. 6A). Banding can be developed throughout the bed or
281 overlying a structureless division (Fig. 6A). The banding is characterised by an alternation
282 between lighter matrix-poor bands and darker matrix-rich bands that comprise bedding parallel
283 millimetric mudstone clast with sharp boundaries (mudstone clast type B) (F8; Fig. 6C).
284 Contacts between bands are diffuse (Figs. 6B and 6F). The spacing between the individual
285 bands (0.5-2 cm) increases from the margin to central parts of the sandstone body (Fig. 8),
286 commonly showing rotation (Fig. 6E). These sandstones develop symmetrical and
287 asymmetrical convolute lamination at bed tops (predominant vergence towards NE; Fig. 6D).
288 Decimetre-scale long and centimetre-scale thick mudstone injections can be observed within
289 this division (Fig. 6B).

290

291 Interpretation: The wedge-shaped and deformed concave-up basal contacts of the sandstone
292 bodies beds in Unit 3 are interpreted to reflect the interaction with the rugose upper surface and
293 syn-sedimentary foundering of sand into the underlying mud-rich debrite (Figs. 6 and 9).
294 Foundering is driven by instability due to the density contrast between the sand deposited above
295 a less dense debrite (density loading) and lateral changes in sediment load (uneven loading)
296 (Owen, 1987, 2003) produced by the short-wavelength rugosity of the upper surface.

297 The lack of sedimentary structures in the lower divisions of bed types recognised in Unit 3 is
298 interpreted as a product of hindered settling from highly-concentrated gravity-flows, resulting

299 in turbulence damping and rapid deposition (Talling *et al.*, 2012), inhibiting any period of
300 traction (Sumner *et al.*, 2008). The normally-graded lower divisions were produced by
301 incremental layer-by-layer deposition from high concentration gravity flows, such as high-
302 density turbidity currents (*sensu* Lowe, 1982). In contrast, the thick-bedded argillaceous
303 sandstones with ungraded mudstone clasts observed in the distal areas (eastern sector) are
304 interpreted as moderate-strength cohesive debrites (*sensu* Talling *et al.*, 2012). The decimetre-
305 scale mudstone clasts (type A) were transported due to the matrix strength of the debris flows
306 and their positive buoyancy with respect to the encasing matrix.

307 The lateral facies transition from high-density turbidites to moderate strength cohesive debrite
308 suggest a flow transformation due to the entrainment of cohesive material from the underlying
309 debrite (e.g. Kane & Pontén, 2012; Baker *et al.*, 2017). The unconsolidated state of the debrite
310 might have enhanced the substrate entrainment of decimetre-scale mudstone clasts (type A)
311 and disaggregation (as indicated by the diffuse boundaries: Fig. 6G), increasing the amount of
312 mud and, therefore, the cohesiveness of the flow. Based on facies juxtaposition, the foundered
313 sandstones can be subdivided into two different facies associations: 1) proximal and 2) distal,
314 foundered sandstones facies associations (Fig. 7). Both high-density turbidites and moderate
315 strength cohesive debrites are characterised by rapid deposition (incremental deposition and en
316 masse freezing, respectively), triggering the liquefaction of the fluid-saturated and
317 unconsolidated upper surface of the debrite and foundering of sand (Fig. 9). The undulations
318 of the concave-up basal interface reflect complex interactions with the substrate: as the denser
319 sand sank into the fluid-saturated muddy substrate, the buoyancy of mud promoted the syn- to
320 post-depositional intrusion (mud diapirs and injectites) of the substrate into sandstones. The
321 most advanced stage of foundering is observed when detached sand-balls develop (Fig. 5;
322 Owen, 2003; Tinterri *et al.*, 2016).

323 In contrast, the banded sandstone characteristic of the upper divisions is interpreted to be
324 formed under episodic near-bed turbulence damping at high rates of deposition (Lowe & Guy,
325 2000). The juxtaposition of the banded sandstones over the mudstone-clast bearing sandstones
326 of the lower divisions suggests highly stratified flows, mixing and upwards transfer of
327 centimetre-scale mudstone clast (type B) and the cohesive material from the disaggregation of
328 the entrained decimeter-scale mudstone clast (type A). This enrichment in cohesive clayey
329 material triggered the periodic suppression of turbulence and, therefore, banding development.
330 The banding passes into convolute laminations towards the top, indicating moderate rates of
331 deposition. The vergence of convoluted laminations suggests a syn-sedimentary shear-stress
332 exerted by the overriding flow (McClelland *et al.*, 2011; Butler *et al.*, 2016) and flow-rebound
333 produced by the underlying debrite relief (e.g. Tinterri *et al.*, 2016).

334

335 **Unit 4**

336 Description: Unit 4 (10-27.3 m thick) has a sharp and concordant contact with the underlying
337 Unit 2 and Unit 3 (Fig. 3). It comprises two subunits: a lower heterolithic interval (Unit 4A)
338 and an upper sandstone-prone interval (Unit 4B; Fig. 2C).

339 *Unit 4A* is thin- to medium-bedded (0.01-0.5 m; Fig 4H) heterolithic succession (F1, F2, F3
340 and F5) with a maximum thickness of 22 m, thinning to 8 m in the central sector above where
341 Unit 2 is thickest (Fig. 3). Most of the thin-beds (0.01-0.1 m thick) are fine- to medium-grained
342 normally-graded sandstones, matrix-poor, moderately well-sorted, and structureless with
343 common planar-parallel lamination and/or starved-ripple lamination near bed tops (F3; Fig.
344 4C). Palaeocurrent measurement shows a consistent flow trend towards the NE (Fig. 9). Unit
345 4A also comprises coarse- to granular normal-graded sandstones, relatively low matrix content
346 with common grain size-breaks (0.07-0.2 m thick), erosive bases and sharp-planar tops (F4;
347 Fig.4D) and two medium-bedded matrix-supported conglomerates with sandstone clasts (F14;

348 0.25 and 0.35 m thick, respectively) that pinch out towards the central sector (Fig. 8). One of
349 these thin gravelly beds, which lacks any lateral thinning or fining trend (Fig. 4I), was traced
350 across the exposure (gravelly marker bed; dashed red line in Fig. 8). In addition, a 0.15 m thick
351 tuff layer (Fig. 4J) was also used for correlation purposes (tuff marker bed; dashed white line
352 in Fig. 3). The medium-bedded sandstones (0.1–0.5 m thick) are structureless, ungraded, with
353 planar-parallel and convolute lamination at bed tops, except one that shows cross-bedding (F6;
354 Fig.4D). These sandstones have sharp bed bases and tops and lack mudstone clasts. In the
355 eastern sector, Unit 4A is dominated by thin- to medium-bedded heterolithic succession that
356 lacks any gravelly (F5) or matrix-supported conglomerate beds (F14).

357 *Unit 4B* (5.7 m thick in the western sector) thins eastwards along a 4.3 km transect until it
358 pinches out, where Unit 2 is thickest (Fig. 3). In the western sector, it dominantly comprises
359 medium- (F5; Fig. 4K) to thick-bedded sandstones (F11; Fig. 4K), with less common
360 "bipartite" sandstone beds (F9 and F10) composed of a matrix-poor lower division and a
361 matrix-rich upper division with mudstone clasts. Conformable bases and sharp tops
362 characterise the thick-bedded sandstones (0.5-1.2 m). Where the thick-bedded sandstones are
363 not amalgamated and are intercalated centimetre-thick beds of fine-grained material (F1 and
364 F2), bed bases are loaded locally. The thick-bedded sandstones are normally graded from
365 medium to fine sand, well-sorted with rare centimetric mudstone clasts at the bed top. Soft-
366 sediment deformation structures, such as centimetre-scale flames with NE vergence, are also
367 common at bed bases and along amalgamation surfaces (Fig. 4L). Banded sandstones are
368 medium-bedded (0.1-0.5 m), fine- to medium-grained, and characterised by alternating
369 between light- and dark-coloured bands, ranging from 0.2 to 2 cm thick (F7; Fig. 4L). Both
370 band types show a similar maximum grain size, although the darker bands are matrix-rich, and
371 light bands are matrix-poor. Banding is generally sub-parallel to bedding. Although banded
372 sandstones are more commonly associated with thick-bedded structureless sandstones, the

373 banded sandstones can be individual event beds, with banding above the structureless basal
374 division. The medium-bedded bipartite sandstone beds (0.1-0.5 m) consist of a medium-
375 grained, matrix-poor and structureless lower division, which is overlain by a fine-grained
376 matrix-rich upper division characterised by poor sorting and abundant mudstone clasts (0.05-
377 0.3 m) with low sphericity and variable roundness (F9 and F10; Fig. 4M). The lower and upper
378 divisions show a gradual upwards increase in matrix content rather than across a sharp
379 boundary. When Unit 4B is traced eastwards towards the central sector, the sandstone package
380 transitions into a few thin-beds (0.1 m thick) of weakly graded, very poorly-sorted matrix-rich
381 sandstone, lacking the mudstone clasts observed in western areas. Unit 4B is absent in the
382 eastern sector.

383

384 Interpretation: In Unit 4A, the thin sandstone beds showing planar and cross ripple laminations
385 support an interpretation as low- to medium-density turbidites (Talling *et al.*, 2012). The
386 starved-ripple lamination observed in thin-bedded sandstones is interpreted as the reworking
387 of sand deposited by dilute flows with low sedimentation rates (Talling *et al.*, 2007; Jobe *et al.*,
388 2012). The intercalation of thin-bedded sandstones with finer-grained deposits suggests a lobe
389 fringe environment (Lobe fringe facies association, Fig. 5) (Prélat *et al.*, 2009; Sychala *et al.*,
390 2017b). The abundant coarse-grained to gravelly thin-bedded sandstones in the western sector
391 record intermittent energetic coarse-grained flows, suggesting sporadic sediment bypass
392 processes (Stevenson *et al.*, 2015). However, the low matrix content within the granular beds
393 suggests a sediment source area where only coarse- to granular grain size was available. The
394 intercalation of such different facies suggests the juxtaposition of depositional environments
395 of contrasting energy and/or different sediment sources. Either scenario could be possible given
396 the complex sediment routing patterns and multiple transverse or axial sources available in the
397 Neuquén Basin during the early post-rift setting (Vicente, 2005; Privat *et al.*, 2021) and by

398 analogy to other post-rift settings (e.g. Lien, 2005; Fugelli, E. M., Olsen, 2007; Hansen *et al.*,
399 2021). The mass failure would trigger a new coarse-grained source due to slide scar position
400 and geometry, promoting intermittent sand supply to an otherwise sand-starved environment
401 (see ‘Origin and role of the Mass-wasting process as a trigger for turbidite systems
402 development’ in discussion). The downdip variability in the thickness of Unit 4A (from 22 to
403 8.5 m thick), reduction in gravelly sandstone content and the stratigraphic thinning between
404 the granular marker bed (red dashed line in correlation) and the top debrite (Unit 2) reveals the
405 existence of subtle relief on the debrite surface (Fig. 3B). Furthermore, the two poorly sorted
406 ungraded muddy sandstones, which are interpreted to be debrites due to their chaotic
407 distribution of clast within the argillaceous matrix, also pinch out towards the central sector.
408 The ripples and convolute laminae with SW vergence (Fig. 3) contrast with the consistent NE
409 paleoflow, suggesting local flow deflection (cf. Tinterri *et al.*, 2016) in the central sector, where
410 the debrite relief is highest, indicating the interaction between sediment gravity-flows and the
411 upper surface of the debrite.

412 Massive medium- to thick-bedded deposits of Unit 4B are interpreted as high-density turbidites
413 formed by incremental layer-by-layer deposition with high aggradation rates (Kneller &
414 Branney, 1995), interpreted to represent proximal lobe axis environments (lobe axis facies
415 association; Fig. 5) (e.g. Prélat *et al.*, 2009; Kane *et al.*, 2017). The location of these facies in
416 the westernmost sector, and the palaeoflow measurements, suggests that the western sector was
417 relatively proximal. Banded sandstones represent the deposits of mud-rich transitional flows
418 formed by tractional reworking (Stevenson *et al.*, 2020). The bipartite beds consisting of a basal
419 structureless to planar laminated sandstone division, overlain by a linked mudstone clast-rich
420 upper division are interpreted as hybrid event beds (HEBs), formed from transitional flows
421 deposited under high-deceleration rates (Haughton *et al.*, 2009; Hodgson, 2009; Kane &
422 Pontén, 2012) in more distal environments than the banded sandstones (Stevenson *et al.*, 2020).

423 The gradual and diffuse boundary between the basal turbidite and the upper debrite suggest
424 vertical segregation of particles within the cohesive flow (Kane *et al.*, 2017). The facies
425 evolution of Unit 4B from proximal (western sector) to distal (eastern sector) of thick-bedded
426 sandstones into hybrid event beds likely represents the downdip transition from lobe-axis/off-
427 axis environments (lobe axis facies association: Fig.5) (sensu Prélat *et al.*, 2009) into lobe-
428 fringe environments (lobe fringe facies association; Fig. 5) (e.g. Kane *et al.*, 2017; Sychala *et*
429 *al.*, 2017a), persisting until the frontal/oblique pinchout (e.g. Hansen *et al.*, 2019).

430

431 **DEPOSITIONAL ARCHITECTURE OF THE DEBRITE AND OVERLYING UNITS**

432 **Large Scale Architecture: Debrite Relief**

433 Using Datum A ('Burro' marker bed), the upper surface of the >9.6 km long debrite forms a
434 broad convex-up relief that reaches a maximum in the central section coincident with the
435 deepest incision (at least 22.5 m of erosional relief; Fig. 3B). The spatial association of the
436 thickest part of the debrite with the deepest incision support a genetic link between the
437 geometry of the flat-ramp-flat shaped basal shear zone and the mounded top. The morphology
438 of the basal surface can buttress material translated downslope and develop positive
439 topographic features, such as pressure ridges (Moscardelli *et al.*, 2006; Bull *et al.*, 2009). Bed-
440 by-bed correlation within Unit 4A shows that where the upper surface of the debrite develops
441 the highest relief (~8 m of positive relief with respect to the western sector), Unit 3 is absent,
442 and it is overlain by Unit 4A (Fig. 3), showing a laterally continuous stratigraphic interval with
443 metre-scale thickness variations (Fig. 8). Unit 4A thins from 22 m (CML-1) and 13 m (CML-
444 2) to 6 m (CML-12) across the highest part of the debrite (Fig. 3B). The lower part of Unit 4A
445 pinches out in the central sector, developing onlaps of individual beds, and supporting the
446 existence of a gentle relief (Bakke *et al.*, 2013; Soutter *et al.*, 2019). In contrast, the upper part
447 of Unit 4A shows tabular architecture with a lateral continuity of over 7 km.

448 Unit 4A is overlain by Unit 4B, which shows a progressive thinning of the submarine lobe from
449 the western to the central sector over 5.6 km, from 5.7 m (CML-3) to 1.7 m (CML-12) and 1
450 m (CML-14) with a mean thinning rate of 0.9 m/km. The submarine lobe pinches out between
451 CML-14 and CML-22 (< 2 km), interfingered with unit 4A (Fig. 3B). The lack of onlap
452 geometries against underlying deposits and subtle thinning rates consistent with unconfined
453 settings (e.g. Prélat *et al.*, 2009) suggests a lack of a pronounced pre-existing relief. However,
454 the coincidence of lobe pinch-out in the area where the debris relief is highest and where the
455 underlying Unit 4A is thinnest might reflect subtle residual relief.

456

457 **Small-Scale Architecture: Foundered Sandstones**

458 The steeply-dipping unconformable base, internal deformation and abrupt thickness changes
459 of Unit 3 sandstones contrast with their flat and conformable tops (see stereoplots in Fig. 6).
460 These sandstone bodies can be subdivided into three different types by their architecture.

461 **Type 1**

462 Description: The thinner founded sandstone bodies range between 0.5- 2 m thick and are only
463 formed by the banded sandstones (Figs. 9A and 9B). They are characterised by 5-25 m wide
464 lenticular shapes, with thickness/width ratios varying from 1:5 to 1:18. These sandstone bodies
465 show relatively constant thinning rates (~0.25 cm/m) towards their pinch outs. They are
466 characterised by: i) advancing onlap terminations onto Unit 2 at the base, and a vertical change
467 into; ii) progressive rotation of laminae and the wedging of the sandstones (Fig. 9C).

468 Interpretation: The onlap termination indicates the interaction between the parental sediment
469 gravity flow and pre-existing debris-related relief (e.g. Bakke *et al.*, 2013), and the sediment
470 load was insufficient to trigger the soft-sediment deformation along the upper surface. In
471 contrast, the overlying rotation and wedging represent growth strata associated with the syn-
472 sedimentary foundering. This juxtaposition of terminations indicates that that foundering did

473 not start since the onset of deposition of sand due to insufficient stress to trigger the soft-
474 sediment deformation. This supports an incremental layer-by-layer deposition of these
475 sandstones rather than the freezing of the parental flow.

476 **Type 2**

477 Description: Thick-bedded foundered sandstones (up to 4 m thick) are characterised by
478 irregular stepped bases and abrupt thickness variations (up to 2 m thinning over 1 m laterally)
479 (Fig. 9D). They are composed by the juxtaposition of two different divisions: i) lower and ii)
480 upper divisions (Fig. 9E). The lower divisions comprise structureless sandstones with poorly-
481 developed amalgamation surfaces (F12 or F13). They rarely exceed 10 m laterally and 3 m in
482 thickness (thickness/width 1:2 to 2:1) and are characterised by both abrupt onlaps terminations
483 and wedging. In contrast, the upper divisions are characterised by banded sandstones (F8),
484 which are more laterally extensive than the underlying division, with a maximum length of 50
485 m and rarely exceed 1 m in thickness, and thin laterally towards margins (thickness/width
486 1:10).

487 Interpretation: The coexistence of onlaps terminations and wedging indicate that the foundering
488 began at the onset of deposition and the existence of pre-existing topography along the upper
489 surface. The sediment load was enough to trigger the foundering because the debrite relief
490 strongly influenced the initial high-concentration flows, which promoted a loss in flow capacity
491 and deposition under high aggradation rates. The rapid deposition and foundering are
492 responsible for the poorly-developed onlap terminations and amalgamation surfaces. The
493 deposition of lower division deposits promoted a reduction in debrite rugosity due to the
494 infilling of topographic lows, enabling the deposition of laterally more extensive deposits. The
495 rotation and wedging in the banding of the upper division is less well developed than in Type
496 1 sandstone bodies. This suggests a progressive reduction in syn-sedimentary deformation and
497 an increase in seafloor stability (e.g. Owen, 1987, 2003).

498 **Type 3**

499 Description: These sandstone bodies show similar facies juxtaposition as in Type 2. In this
500 case, the sandstones terminate against heterolithic megaclasts due to their preferential location
501 towards the top of the debrite (Figs. 5, 9F). In these cases, the geometries of the foundered
502 sandstones diverge from the concave-up geometry, dependent on the shape of the megaclast.
503 Some megaclasts disconnect bodies laterally, whereas others only impact the base, with the top
504 part of the sandstones undisturbed (Fig. 9G). Interpretation: The fluid-saturated matrix and
505 rigid megaclast respond differently to the shear stress exerted by the deposition of sand
506 creating. This differential compaction (Ogata *et al.*, 2014b) controls the architecture of the
507 foundered sandstones, creating complex bodies (Fig. 9H).

508 **DISCUSSION**

509 **Basal Shear Zone And Impact On The Substrate**

510 As submarine landslides travel across the seafloor, they exert shear stress on the substrate,
511 coupled with significant over-pressure (Bull *et al.*, 2009; Hodgson *et al.*, 2019; Payros &
512 Pujalte, 2019). This leads to substrate entrainment (Eggenhuisen *et al.*, 2011; Hodgson *et al.*,
513 2019) and/or deformation (Butler & McCaffrey, 2010; Watt *et al.*, 2012; Dakin *et al.*, 2013;
514 Ogata *et al.*, 2014b). The debris flow (Unit 2) incised at least 22.5 m into the substrate (Unit 1;
515 Fig. 3). In the central sector, the basal shear surface forms ramps (up to 800 m long, $>2^\circ$) and
516 flats (up to 1550 km long; Fig 3B; between the logs CML-9 and CML-10) (see Lucente & Pini,
517 2003; Martinez *et al.*, 2005 for flat-ramp-flat geometry). The stress applied to the substrate
518 during the emplacement is accommodated by both stratigraphic intervals consisting of
519 deformed packages (basal shear-zone) and interfaces consisting on a plane (basal shear-
520 surface) (Alves & Lourenço, 2010), such as the discrete basal shear zone located in upper Unit
521 1. The absence of contractional features in the deposits underlying Unit 1 supports the
522 deformation as the result of the shear stress produced by the emplacement of the debrite rather

523 than tectonism. The basal shear zone has variable thickness and deformation styles. It is absent
524 in the western sector, whereas erosion and deformed intervals record a high degree of basal
525 shear stress in the central sector (Fig. 3B). In the central sector, the deformed package (up to
526 10 m thick) is characterised by decametre-scale thrusts with metre-scale offsets and drag
527 folding(Fig. 4B). The predominance of imbricate thrusting over folding, and lack of internal
528 disaggregation within the package, indicate competent substrate rheology (e.g. Van der Merwe
529 *et al.*, 2011). The eastward vergence of the compressional structures (Fig. 4B) indicates an
530 eastward emplacement direction for the debris flow (Twiss & Moores, 1992), consistent with
531 the palaeoflow indicators in the bounding strata.

532 The thrusting is attributed to bulldozing by the entrenched debris flow (e.g. Jackson, 2011;
533 Hodgson *et al.*, 2019; Payros & Pujalte, 2019), representing the initial stage of substrate
534 entrainment. Entrainment of megaclasts into a debris flow has been reported in other systems
535 in the subsurface (Moscardelli *et al.*, 2006; Alves & Cartwright, 2009; Sawyer *et al.*, 2009;
536 Dakin *et al.*, 2013; Ortiz-Karpf *et al.*, 2015; Soutter *et al.*, 2018; Nwoko *et al.*, 2020a) and more
537 rarely at outcrop (Ogata *et al.*, 2014b; Sobiesiak *et al.*, 2016; Hodgson *et al.*, 2019;
538 Cumberpatch *et al.*, 2021). The progressive increase in thickness and degree of strain along the
539 basal shear zone of Unit 2 and the enrichment in rafted heterolithic megaclasts (Fig. 3B and 5)
540 suggest downdip evolution of the debris flow, which might have affected the parental debris
541 flow rheology (e.g. Hodgson *et al.*, 2019; Payros & Pujalte, 2019) and bulking of the flow (Gee
542 *et al.*, 2006; Alves & Cartwright, 2009; Butler & McCaffrey, 2010; Hodgson *et al.*, 2019). The
543 preferential location of heterolithic megaclast towards the top of Unit 2 might be related to
544 internal granular convection cells created along with the debris flow, enhanced by the buoyancy
545 of less dense rafted megaclast compared to debrite matrix (Hodgson *et al.*, 2019) and kinetic
546 sieving (Legros, 2002). In contrast, conglomerate megaclast are always found at the base of
547 the debrite due to their higher density than the surrounding debrite matrix.

549 Dynamic Debrite Topography And Impact On Overlying Strata

550 The absence of Unit 3 sandstones over the thickest part of the debrite suggests that the sediment
551 gravity flows were strongly stratified and influenced by the debrite relief (Fig. 8). The
552 sandstone bodies are also disconnected at finer scales, revealing short wavelength (metre-scale)
553 and amplitude (decimetre-scale) rugosity on the debrite surface. The existence of simultaneous
554 short wavelength and amplitude rugosity superimposed on a large-scale wavelength relief on
555 the upper surface of an MTD has also been reported by Armitage *et al.* (2009), defined as
556 'surface-topography hierarchy', in the Cretaceous Tres Pasos Formation at the Sierra Contreras
557 (Chile) and by Fairweather (2014) in Carboniferous Paganzo Basin at Cerro Bola (Argentina).
558 In this study, the deposition of sand in pre-existing lows filled the short-wavelength rugosity
559 and triggered the loading of individual sandstone bodies onto the mud-rich debrite (See 'Small-
560 scale architecture: Foundered sandstones' sections), leaving the large-scale relief underfilled
561 (Figs. 3 and 8). The foundering process is evidence of substrate liquefaction and highlights the
562 dynamic interface between the debrite and subsequent flows and their deposits. A similar
563 scenario was proposed by Van der Merwe *et al.* (2009, 2011) in the Vischkuil Formation in the
564 Laingsburg depocentre (Karoo Basin).

565 The ability of supra MTD rugosity to pond turbidity currents travelling across their upper
566 surface is a well-known phenomenon (Kneller *et al.*, 2016). However, the presence of Unit 3
567 foundered sandstones up-dip and down-dip of the debrite high (Fig.3B), and its consistent NE
568 paleocurrent trend, suggest connected sediment transport routes across the debrite with no
569 evidence of flow ponding or stripping (e.g. Armitage *et al.*, 2009; Fairweather, 2014). The
570 highly-stratified grown-hugging parental flows of Unit 3 would have been ponded in proximal
571 parts (western sector) if a fully enclosing topography existed given their reduced ability to
572 surmount obstacles (Al-Ja'Aidi *et al.*, 2004; Bakke *et al.*, 2013), resulting in sand starvation

573 over the debrite in distal settings (Sinclair & Tomasso, 2002; Kneller *et al.*, 2016). The
574 overlying Unit 4A can be traced laterally across the study area, with metre-scale thinning where
575 the debrite is thickest (see CML-12; Fig. 3). Apart from this, the advancing onlap geometries
576 of the thin beds and the divergence in the overall NE-orientated paleocurrents (rose diagram
577 Unit 4; Fig. 3) indicate the progressive healing of the large-scale wavelength debrite relief,
578 with some deflection of turbidity currents (Fig. 10).

579 The thin sandstone beds of the upper part of Unit 4A healed the debrite high. However, the
580 gravelly beds thin and fine from proximal to distal areas (western to eastern sectors), and the
581 two debrites pinch out in proximal areas (western sector), suggesting subtle remnant
582 topography (Fig. 8). The different lateral continuity of individual beds is explained by different
583 rheologies of individual sediment gravity flows, which affect the flow efficiency (Al Ja'Aidi
584 *et al.*, 2004). Cohesive debris flows are more influenced by irregular relief, while low-density
585 turbidity currents are less affected by seafloor topography (Bakke *et al.*, 2013; Soutter *et al.*,
586 2019). This suggests that laterally continuous thick accumulations of lobe fringes can develop
587 on gentle topographies, while the submarine lobes' axial parts were restricted to lower relief
588 areas. The interaction of thin-bedded turbidites successions with gentle topography has also
589 been reported in other deep-water settings (i.e., 'aggradational lobe fringes'; Sychala *et al.*,
590 2017b). The deposition of lobe fringe successions reduced confinement, which enabled the
591 deposition of the Unit 4B submarine lobe.

592 The submarine lobe is characterised by a progressive thinning and fining, developing pinch-
593 out geometries and interfingering with Unit 4A in the area where the relief of the debrite is
594 highest. The development of pinch-out geometries over the areas where the debrite shows a
595 mounded relief and where the Unit 4A onlaps and thins suggests that the relief was not wholly
596 healed with the deposition of Unit 4A and affected the parental flows of Unit 4B.

597 One explanation is that the exposure exhumes the Unit 4B lobe obliquely, with the medium- to
598 thick-bedded lobe axis deposits in the westernmost sector (CML-1 to CML-4) transitioning
599 into an HEB-dominated fringe, being highly impacted by gentle seafloor topography (Soutter
600 *et al.*, 2019; Privat *et al.*, 2021). Alternatively, the seafloor relief could have promoted the
601 modification of flow pathways and deflection of flows, thus changing the downdip orientation
602 (Fig. 8). All these scenarios suggest a confined and uncontained (see Southern *et al.*, 2015)
603 lobe-type depositional system. The precise dispersal pattern of the flows remains unknown due
604 to the outcrop limitations. Nonetheless, the documented stratigraphic evolution reveals that
605 long-lived debrite relief and progressive healing by deposition of aggradational lobe fringes
606 enabled the progradation of sand-rich submarine lobe, albeit with changes in flow rheology the
607 bed style and element-scale pinchout (Fig. 8).

608 Another explanation is that the debrite relief in the central sector might have been rejuvenated
609 through volume changes in the debrite due to differential compaction by loading the lobe itself
610 in the proximal sector through fluid loss or fault-controlled mechanical subsidence. However,
611 it seems unlikely that the deposition of a 5.7 m thick lobe could promote a volume loss in an 8
612 – 47 m thick debrite, given that both units are separated by 8 – 22 m thick thin-bedded interval.
613 In contrast, the other two hypotheses are more plausible. Fluid loss-controlled evacuation could
614 have promoted the subsidence of the upper surface of the debrite and overlying units (e.g.
615 Browne *et al.*, 2020). Alternatively, given the early post-rift setting, mechanical subsidence by
616 an east-facing and N-S striking fault (Manceda & Figueroa, 1995) could have generated more
617 accommodation in the western part of the study area (see Cristallini *et al.*, 2006). However,
618 this implies a very localised and rapid reactivation, and there is no other evidence for post-rift
619 tectonism identified.

620

621 **Origin And Role Of The Mass-Wasting Process As a Trigger For Turbidite Systems**

622 **Development**

623 The emplacement of the >9.6 km long and erosional debrite in the Chacay Melehue depocentre
624 reflects an abrupt change in sedimentation patterns, which were previously dominated by dilute
625 mud-rich flows (Unit 1). The first significant sand influxes in the depocentre for ~6 Myr since
626 the Aalenian (interval II of Gulisano & Gutiérrez Pleimling, 1995) are recorded by the sand-
627 rich deposits (Unit 3) immediately overlying the debrite (Fig. 10). The juxtaposition of sand-
628 rich turbidites over debrites (metres to hundreds of meters thick) have been reported in other
629 systems (Kleverlaan, 1987; Labaume *et al.*, 1987; Payros *et al.*, 1999; Fallgatter *et al.*, 2017).
630 These authors suggest that the debris flow underwent a period of mixing with ambient water,
631 leading to the generation of an overriding co-genetic turbidity current. The foundering
632 phenomenon reported here reveals a close spatiotemporal relationship between the debrite
633 emplacement (Unit 2) and overlying sandstone deposition (Unit 3). An alternative mechanism
634 is that the mass-failure event altered the basin margin physiography such that a sand source
635 was captured. Mass-wasting processes responsible for the evacuation of material from shelf
636 edge and upper slope areas alter the bathymetric configuration of basin margins and promote
637 the funnelling of sediment stored in shallow marine environments through slide scars (e.g.
638 Moscardelli & Wood, 2008; Kneller *et al.*, 2016; Steventon *et al.*, 2020) (Fig. 11). The role
639 played as a trigger mechanism for sand delivery into deep-water setting by the mass-wasting
640 event is a plausible scenario given the sand-starvation recorded in the coeval deposits of Los
641 Molles Fm along the eastern margin of the Chacay Melehue depocentre (Veiga *et al.*, 2013)
642 Given the palaeoflow and kinematic indicators, the thickness patterns of the studied units (Fig.
643 3B), and previous studies on sediment supply from the volcanic arc (Vicente, 2005), we
644 propose that the mass failure originated to the west of Chacay Melehue, where a major syn-rift
645 fault is located close to the volcanic arc (<30 km; Manceda & Figueroa, 1995; De La Cruz &

646 Suarez, 1997; Vicente, 2005). The role of the western volcanic arc as a source area for the early
647 post-rift sediment supply in the Chacay Melehue depocentre is supported by the southeastwards
648 directed paleocurrents measured in the Aalenian turbidite system at the base of the Los Molles
649 Formation (Vicente, 2005; Fig. 2) and the abundance of pyroclastic deposits within Los Molles
650 Formation stratigraphy (Zöllner & Amos, 1973; Rosenfeld & Volldaeimer, 1980; Gulisano &
651 Gutiérrez Pleimling, 1995; De La Cruz & Suarez, 1997; Llambías & Leanza, 2005). The oyster-
652 bearing conglomerate megaclast and well-rounded volcanic epiclast within the matrix of the
653 debrite reflect long-lived reworking in shallow-marine settings prior to the mass failure,
654 suggesting a shallow-water origin or remobilization of older slope strata, including shallow-
655 marine deposits. This could represent the downslope transfer of sand following the collapse of
656 reworked volcanoclastic deposits along the magmatic arc (Fig. 9). The evolution from the initial
657 mass-wasting sediment supply responsible for erratically distributed founder sandstone
658 bodies (Unit 3) to a more mature system with the subtle distribution and diversity of lobe
659 architectural elements (Unit 4) reflects the evolution to a more organised sediment supply
660 system (Fig.10). This is abruptly superseded by a return to sand-starved conditions with
661 dominant dilute mud-rich flows and hemipelagic deposition until the end of the Lower
662 Callovian (Gulisano & Gutiérrez Pleimling, 1995).

663

664 **CONCLUSIONS**

665 We document the anatomy and architecture of a >9.6 km long exhumed debrite and show how
666 its twofold short- and long-wavelength relief and composition provided a likely input route for
667 the subsequent sand-rich deep-water system and influenced flow behaviour depositional
668 patterns. The basal surface of the debrite forms ramps and steps, indicating deep incision and
669 entrainment of the substrate that includes megaclasts. The foundering of overlying sands, their
670 resultant geometry and spatial distribution, and the down-dip increase in mud content, indicate

671 a dynamic and rugose upper surface to the debrite and complex flow-deposit interactions. The
672 spatial distribution of the foundered sandstones indicates ground-hugging flows and the
673 existence of debrite relief, which was progressively but not entirely healed by the submarine
674 lobe. However, the architecture and facies distribution of the submarine lobe and their parental
675 flows were still impacted by the long-lived, possibly rejuvenated, debrite-related topography.
676 The debrite emplacement coincided with an abrupt change in sediment supply to the Chacay
677 Melehue depocentre from long-term mud-rich sedimentation to a transient sand-rich system.
678 This change in depositional character is interpreted to have resulted from the funnelling of
679 sediment stored in shallow marine environments to the west through a slide scar created by the
680 debris flow, thus reconfiguring the sediment delivery pathway. Therefore, this study highlights
681 that basin margin mass failures and their deposits play a key role in sediment dispersal patterns
682 into deep-water settings, as well as the behaviour of subsequent sediment gravity flows
683 travelling across their upper surface.

684

685 **ACKNOWLEDGEMENTS**

686 This study is a collaboration between The University of Manchester (UK), The University of
687 Leeds (UK), Leibniz University (Germany), The University of Liverpool (UK) and Centro de
688 Investigaciones Geológicas (CIG) (Argentina). The authors would like to thank the local
689 farmers of the Chacay Melehue region of Argentina for permission to carry out field studies on
690 their land. The LOBE 3 consortium project of which this research forms a part is supported by
691 sponsorship from Aker BP, BHP, BP, Equinor, HESS, NEPTUNE, Petrobras, PetroChina,
692 Total, Vår Energi and Woodside, for which the authors are grateful.

693

FIGURES

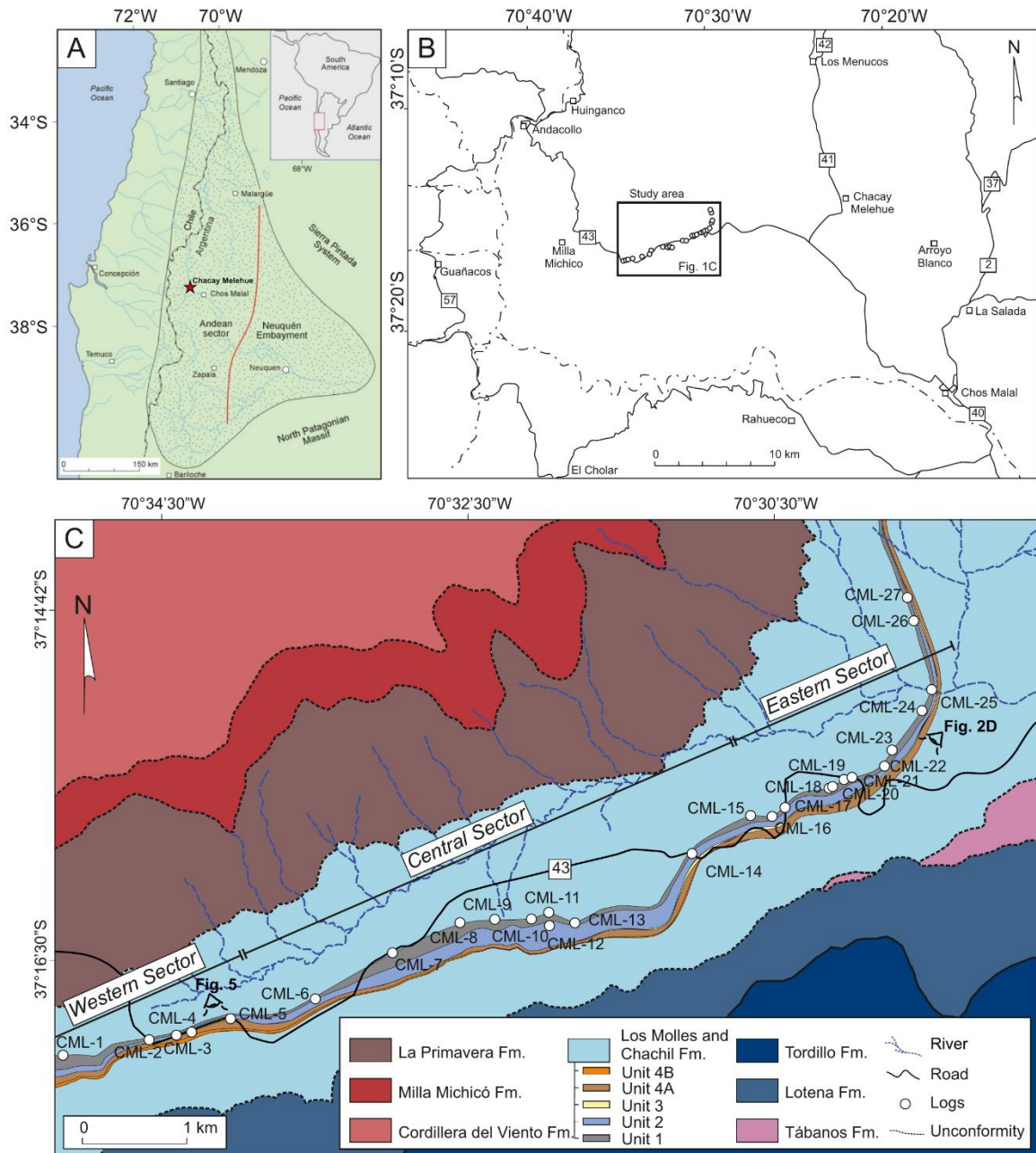


Fig. 1. (A) Location map of the Neuquén Basin and the study area Chacay Melehue (red star). (B) Local location map of the study area. (C) Map of the Chacay Melehue area with the formations (modified from Llambías *et al.* (2007)) and the locations of the logs. See the studied units and their distribution.

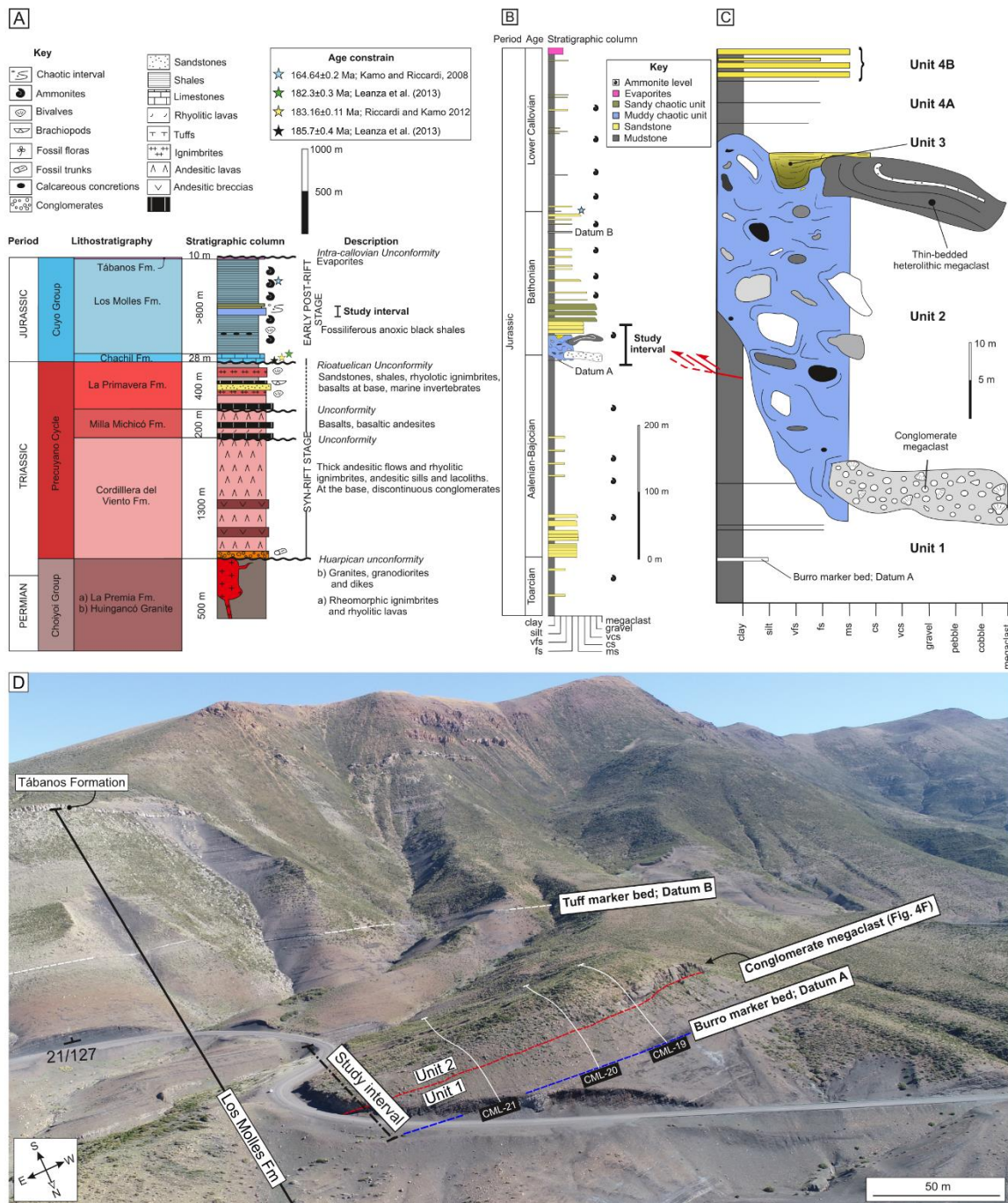


Fig. 2: (A) General stratigraphic column of Chacay Melehue showing the Los Molles Formation (modified after Gulisano and Gutiérrez-Pleimling (1995) and Llambias (2007) and Leanza et al. (2013)). (B) Stratigraphic column of Los Molles Formation and the Tábanos Formation in the Chacay Melehue area (modified after Gulisano and Gutiérrez-Pleimling (1995)). (C) Schematic log of the study interval (D) Panoramic view from UAV photograph (cars on the road for scale) showing the deep-water Los Molles Formation overlain by evaporitic deposits of the Tábanos Formation. The study interval and the two datums used to constrain the base and top of the correlation panel are shown. See the location of logs 19, 20 and 21 (Fig. 3A).

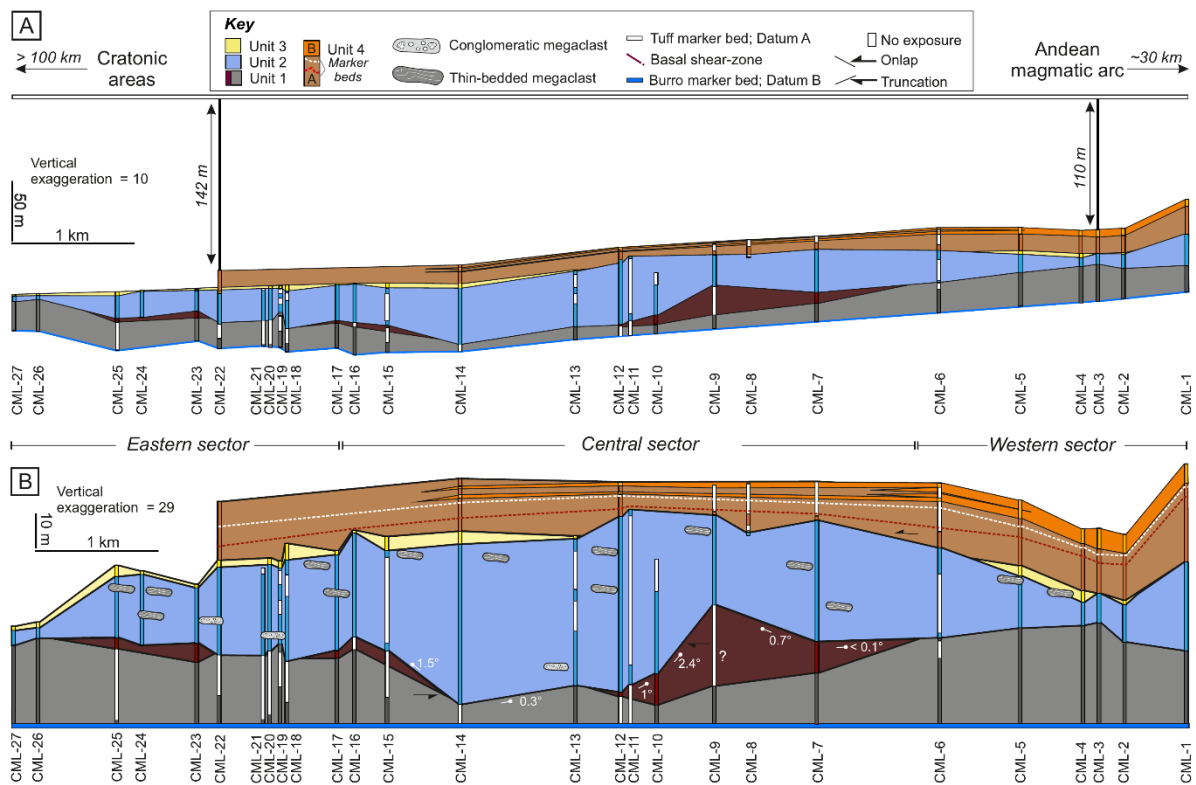


Fig. 3: Correlation panels showing the spatial relationship between stratigraphic units in the Bathonian succession of the Los Molles Formation and the different depositional architectures constrained by flattening on the top and basal datums. (A) Correlation panel including Units 1 to 4 with the Tuff marker as a datum (Datum B) showing the step-like geometry of the slope. (B) Correlation panel with the basal Burro marker bed (Datum A) as a datum showing the complex ramp-flat geometry and the basal-shear zone elements (brown coloured zone) at the base of Unit 2 and the correlation within Unit 4A based on two continuous sandstone marker beds. Note the heterogeneous distribution of Unit 3 and the pinching of Unit 4B in the central sector.



Fig. 4: Representative sedimentary facies photos. (A) Unit 1: Planar-laminated mudstone (F1) with a few thin- to medium-bedded intercalated siltstone beds (F2) (Burro marker bed; Datum A) and sandstone beds (F5). (B) Unit 1: Basal shear-zone characterised by imbricated thrusts with drag folding. (C) Unit 4A: Heterolithic deposits consisting in the alternation between siltstones (F2) to (very) fine-grained sandstones (F3). (D) Unit 4A: Gravelly thin bed (F4)

locally eroded into fine-grained sandstones (F3). (E) Unit 4A: Medium-bedded sandstones with cross-bedding (F6). (F) Unit 2: 140 m long conglomerate megaclast, bearing oyster and belemnite fragments, and sitting above Unit 1. See a fragment of an oyster in the inset (G). (H) Unit 2, 3 and 4A: Foundered sandstones onlapping the matrix-rich debrite (F14) with deformed heterolithic megaclasts draped by the thin-bedded deposits of Unit 4A. (I) Unit 4A: Gravelly and (J) Tuff-marker bed within 4A. See the correlation figure 3B and 8 (red and white dashed lines). (K) Unit 4B: Amalgamated medium- (F6) to thick-bedded (F11) sandstones. (L) Unit 4B: Medium-bedded banded sandstone (F7) overlain by massive matrix-poor sandstones (F5). Note the vergent flame structures within the amalgamation surface (M) Unit 4B: Thin- (F9) and medium-bedded (F10) hybrid event beds type 2 (cf. Haughton et al., 2009) with a linked debrite consisting of matrix-rich sandy division with elongated mudstone clasts.

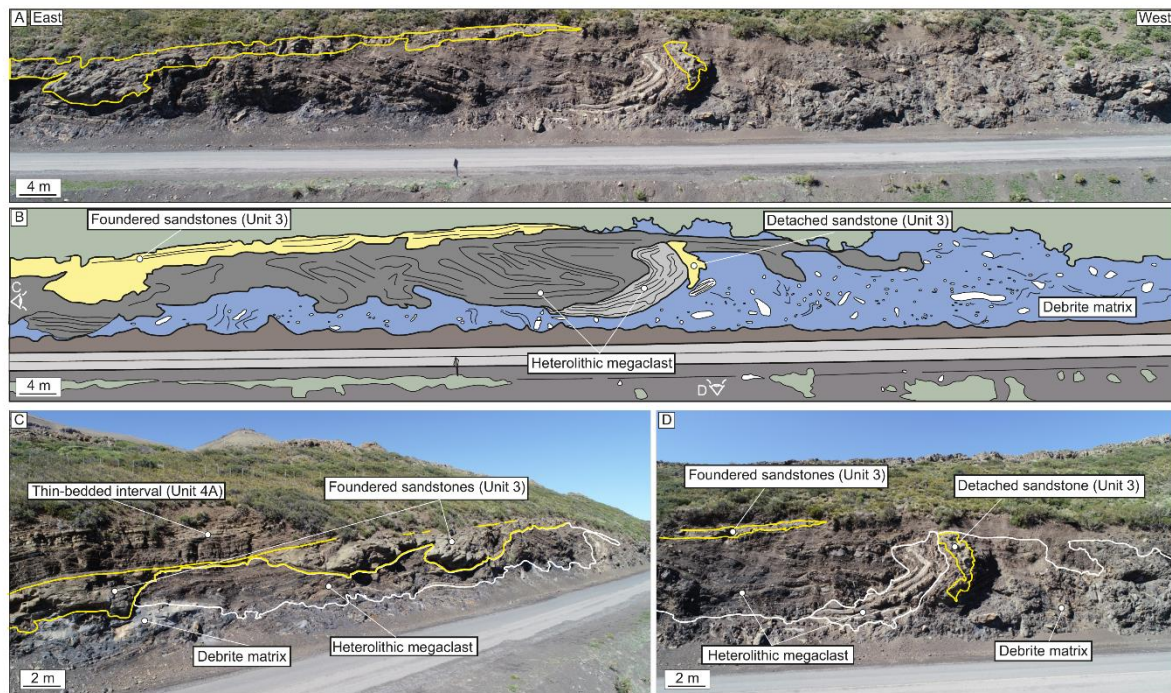


Fig. 5: (A) Panorama of the exposure showing the upper division of Unit 2 overlaid by Unit 3 foundered sandstone. (B) Sketched exposure of A. Note the matrix-supported texture and the chaotic distribution of clasts. (C) and (D) Same exposure of A from a different perspective. Note the unconformable base and conformable flat top interface of Unit 3 sandstones. See B for location.

LITHOFACIES	LITHOLOGY	DESCRIPTION	THICKNESS	PROCESS INTERPRETATION
F1: Laminated mudstone.	Mudstone.	Dark-coloured planar parallel laminated mudstone with Ammonites. Concretionary horizons are common.	0.1-3 cm	Deposits from very dilute sediment gravity under relative dysoxic-anoxic conditions (Trabucho-Alexandre <i>et al.</i> , 2012; Könitzer <i>et al.</i> , 2014).
F2: Graded siltstone.	Graded siltstone.	Normally-graded from silty bases to mud-rich tops. Usually structureless, although planar parallel-laminations are common.	1-5 cm	Deposition under low-density turbidity current (Allen, 1971).
F3: Thin-bedded fine-grained sandstones.	Very fine- to fine-grained sandstones.	Normally-graded, well-sorted thin-beds. Fine-grained bases and very fine-grained tops. Structureless at the base with planar laminated tops. Rare starved ripple lamination at bed tops.	1-10 cm	Deposition and tractional reworking by low-density turbidity current (Allen, 1971, 1982; Jobe <i>et al.</i> , 2012).
F4: Thin-bedded granular sandstones.	Granular- to medium-grained sandstones.	Normally-graded, very well-sorted, coarse-grained to granular- sandstones. Sharp planar base and top.	1-10 cm	Deposition from turbidity currents.

F5: Medium-bedded sandstones.	Very fine- to medium-grained sandstone.	Structureless, normally-graded sandstones. Bed bases are medium-grained, grading up until fine-grained.	10-50 cm	Deposition from medium-density turbidity currents. High-aggradation rates inhibited the formation of sedimentary structures (Talling <i>et al.</i> , 2012).
F6: Thin-bedded cross-stratified sandstones.	Granular- to medium-grained sandstones.	Normally-graded, well-sorted thin-beds. Foreset heights range from 5 to 7 cm, and angles vary between 10° and 35°. Erosional bases are common—sharp contacts, with planar base and undulatory top.	5-10 cm	Deposition and tractional reworking by turbidity currents (Tinterri, 2011).
F7: Medium-bedded banded sandstones.	Banded sandstones with sharp alternation between darker and lighter bands. Lighter bands are grain-supported, while darker	Sandstones comprising alternation between matrix-poor light bands and matrix-rich dark bands (0.2 to 2 cm thick). Similar grain size (fine to medium) along with different bands. Heterolithic bedforms and pinch-and-swell geometries can be developed. The bed bases can be structureless.	10-50 cm	Deposits beneath mud-rich transitional plug flow formed by tractional reworking within the upper stage plane bed flow regime (Baas <i>et al.</i> , 2009, 2011, 2016; Stevenson <i>et al.</i> , 2020).

	bands are matrix-supported and lack mudstone clasts.			
F8: Thick-bedded banded sandstones with mudstone clast.	Banded sandstones with diffuse alternation between darker and lighter bands. Lighter bands are grain-supported, while darker bands are matrix-supported, with abundant mudstone clasts.	Sandstones comprising banding between matrix-poor light bands and matrix-rich mudstone clast (millimetric scale) bearing dark bands (0.5-2 cm). Banding is diffuse and can be developed throughout the bed or from the middle to the top parts of a bed, commonly overlaid by convolute lamination. Laminae show local tilting and increasing spacing between laminae.	50-150 cm	Rapid aggradation and episodic damping of near bed turbulence due to clay floccs disaggregation (Lowe & Guy, 2000). Increasing spacing between laminae is attributed to growth strata due to foundering processes.
F9: Thin-bedded hybrid event beds.	Silty sandstone.	Matrix poor bases with linked argillaceous, ungraded and poorly-sorted top divisions.	1-10cm	Distal deposits are the product of en masse deposition and potentially behaving as transitional to laminar flows (Kane <i>et al.</i> , 2017).
F10: Medium-bedded hybrid event beds.	Bipartite sandstones with matrix-poor basal divisions and upper argillaceous	Bipartite sandstone beds are characterised by a matrix-poor structureless lower division passing	10-50 cm	Deposits formed under transitional flows. Erosion and incorporation of intrabasinal clasts. The entrained substrate was rapidly disaggregated within the flow resulting in

	mudstone-clast prone division.	gradually into linked mudstone clasts matrix-rich upper division.		clast-rich and clay-rich divisions at the bed top. The flows increased in concentration but had not developed stable density stratification (Haughton <i>et al.</i> , 2003; Davis <i>et al.</i> , 2009; Hodgson, 2009; Kane & Pontén, 2012; Kane <i>et al.</i> , 2017).
F11: thick-bedded sandstones.	Structureless sandstone.	Structureless, thick-bedded argillaceous sandstones, lacking mudstone clasts. High amalgamation rations and erosional beds when lying above fine-grained intervals. Banding is locally developed at bed tops, alternating between matrix-poor light bands and matrix-rich dark bands (0.2 to 2 cm thick). Similar grain size (fine to medium) along with different bands. Heterolithic bedforms and pinch-and-swell geometries can be developed.	0.5-1.2 m	Deposition under high-density turbidity currents (sensu Lowe, 1982), formed by incremental layer-by-layer deposition with high aggradation rates (Kneller & Branney, 1995; Sumner <i>et al.</i> , 2008; Talling <i>et al.</i> , 2012). The banding represents planar lamination (Bouma Tb division) (Stevenson <i>et al.</i> , 2020).
F12: Thick-bedded structureless matrix-poor sandstones with	Structureless sandstones with a mudstone clast at the base.	Structureless thick-bedded, medium- to coarse-grained, crudely normally-graded sandstones, with low-matrix content. They contain some mudstone	0.5-2 m	Deposition under high-density turbidity currents (sensu Lowe, 1982), formed by incremental layer-by-layer deposition with

normally-graded mudstone clast.		clasts (0.1-1 m) with diffuse boundaries preferentially located at the base, which show coarse tail grading. Mudstone diapirs along the basal interface are common.		very high aggradation rates (Kneller & Branney, 1995; Sumner <i>et al.</i> , 2008; Talling <i>et al.</i> , 2012). Mudstone clast is entrained due to erosion of an unconsolidated debrite (Unit 2) and syn-sedimentary buoyancy product of density instabilities (Owen, 1987, 2003).
F13: Thick-bedded structureless matrix-rich sandstones with ungraded mudstone clast.	Argillaceous sandstone with abundant mudstone clasts.	Structureless thick-bedded, fine- to medium-grained, ungraded sandstones with very high matrix content and abundant decimetric mudstone clasts (0.1-1 m) randomly distributed.	0.5-2 m	Moderate-strength cohesive debris flows derived from mudstone clast entrainment and disaggregation. Mudstone clasts are supported by their positive buoyancy with respect to the surrounding matrix and the matrix strength (Talling <i>et al.</i> , 2012).
F14: matrix-supported conglomerates.	Mud-rich medium-grained sandstone to sandy mudstone.	Poorly sorted, ungraded with a chaotic distribution of outsized clasts (up to 140 m long). Irregular and sharp contacts. Bases can be erosive and undulatory tops.	7.4 – 47.9 m	Cohesive debris-flow deposits (sensu Talling <i>et al.</i> , 2012).

				with near-instantaneous deposition from a flow with high yield strength and buoyant support.
--	--	--	--	--

Table 1.—Descriptions of the facies recognised in the Los Molles stratigraphy of the Chacay Melehue area, including lithologies, thicknesses, and interpretations of their depositional processes.

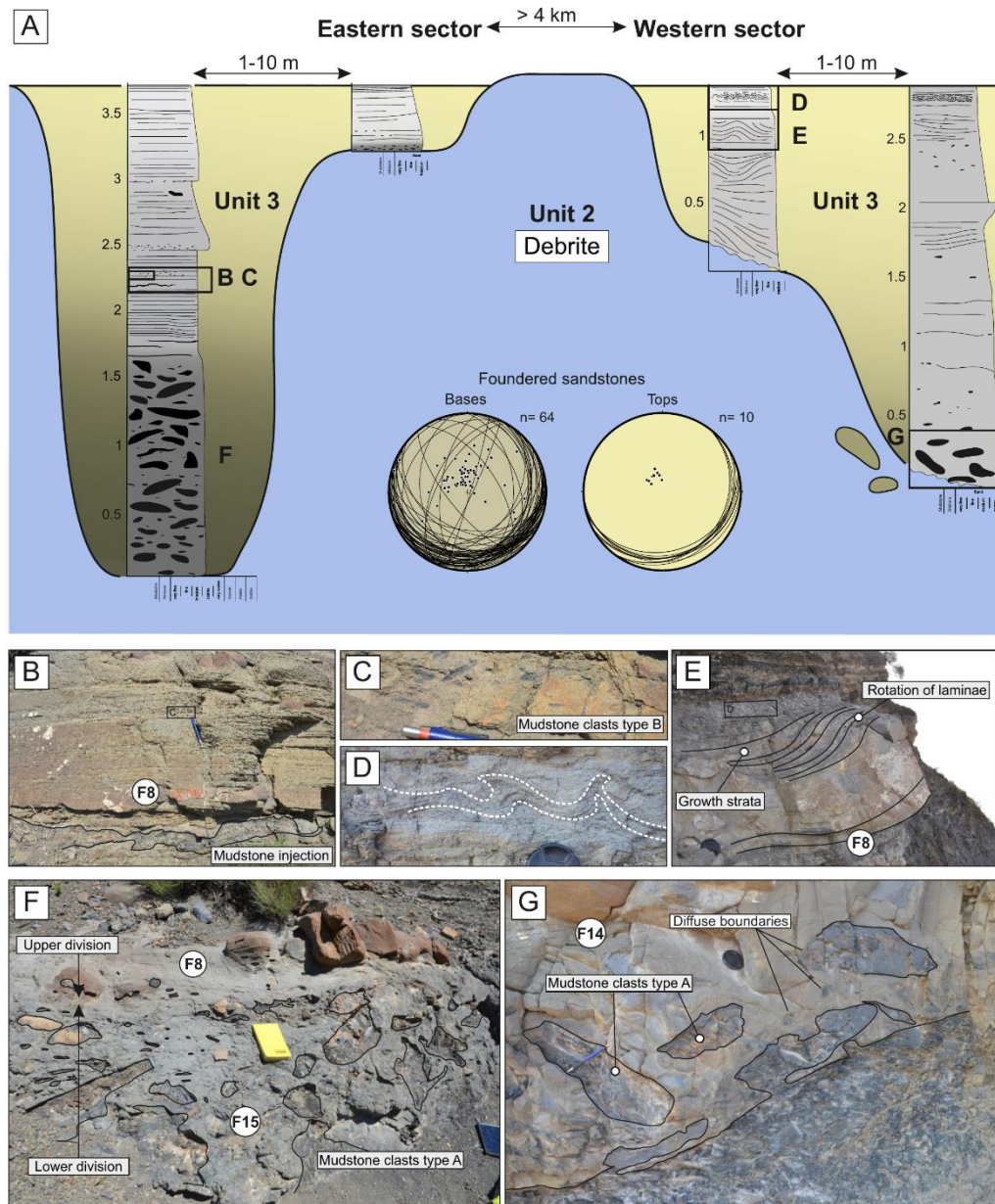


Fig. 6: Foundered sandstones (Unit 3) diagram. (A) Illustrative correlation of sandstone foundering (Unit 3) into debrite (Unit 2). Note the difference between the conformable bed tops of matrix-poor and traction dominated sandstones (right-hand stereonet) and the mudstone clast- and matrix-rich sandstone texture near the unconformable bed bases (left-hand stereonet), which shows the architecture of these sandstone bodies. (B) Thick-bedded banded sandstones with bedding-parallel sill injection (F8). See mudstone clasts (type B) in the inset (C). (D) Convolute-laminae with NE vergence. (E) Sandstones showing rotation and growth strata. (F) Lower division comprising thick-bedded structureless argillaceous (F13) sandstone division with a patchy and random distribution of mudstone clasts overlain by upper division

comprising thick-bedded banded sandstones (F8). (G) Thick-bedded structureless sandstone with an undulating irregular base comprising decimetre-scale mudstone clasts (type A) (F12).

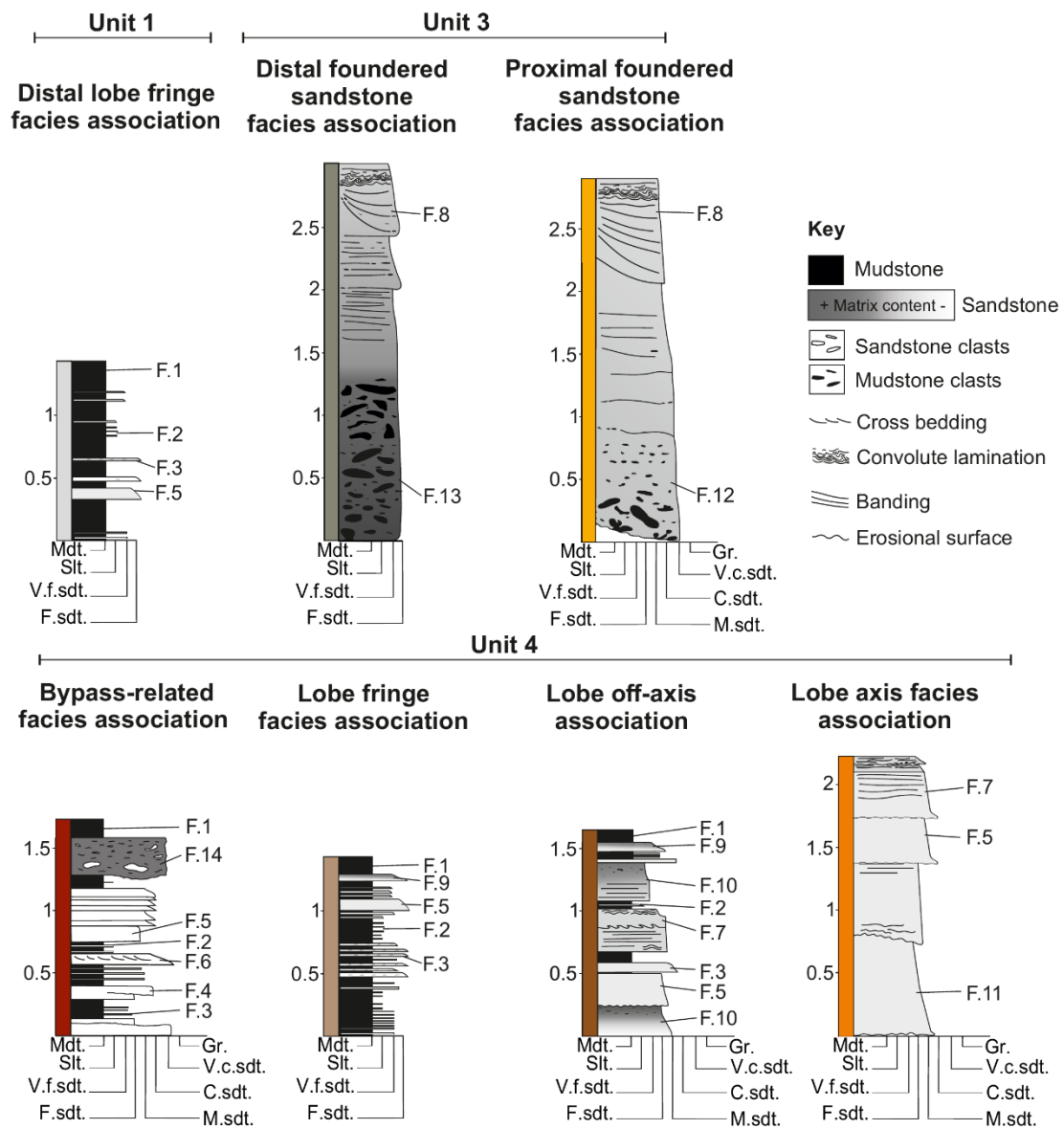


Fig. 7. Facies associations of Units 1, 3 and 4. See table 1 and Figs. 4 and 6 for more detail. See Fig. 8 for the lateral variability of each facies association.

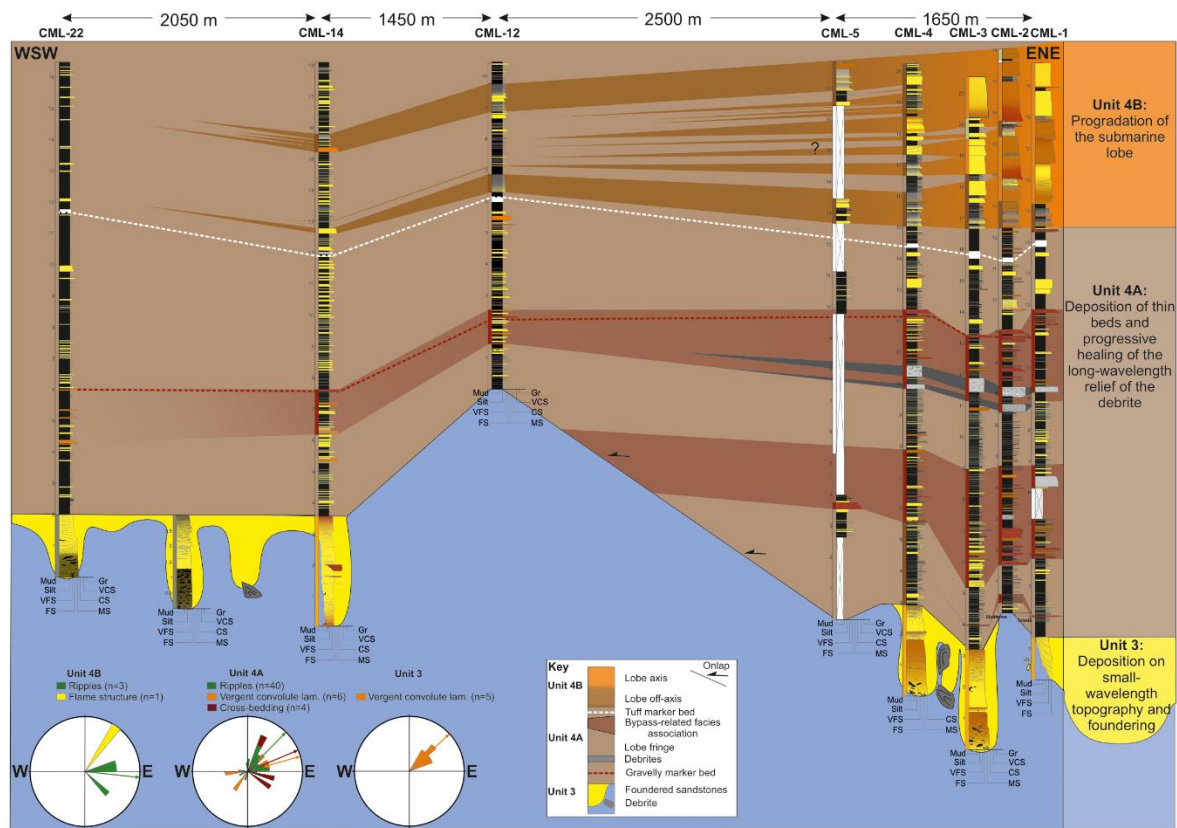
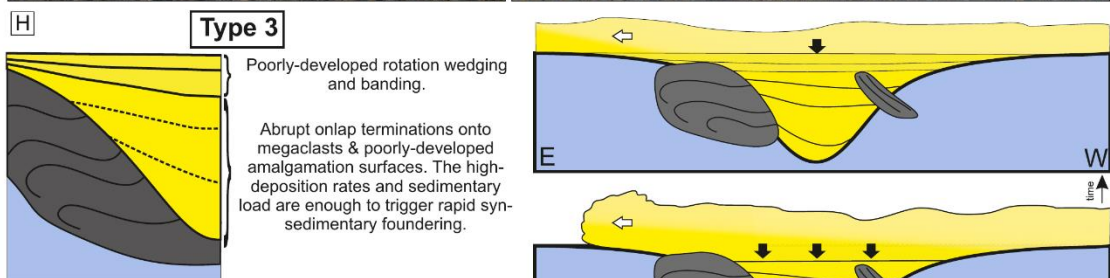
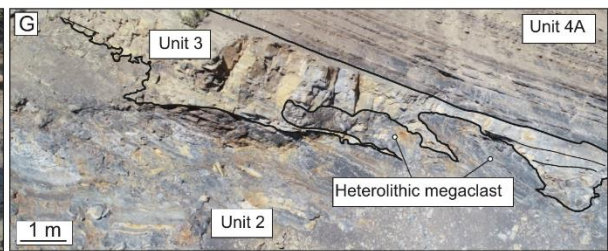
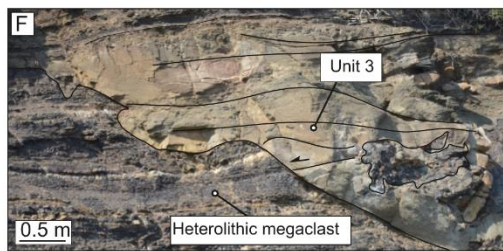
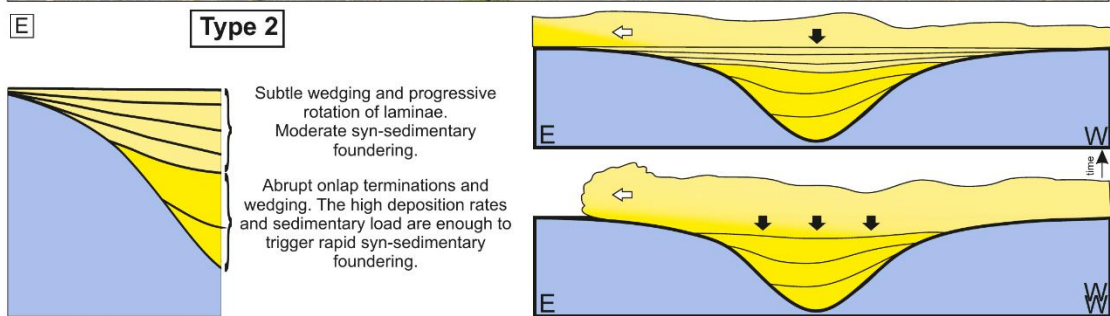
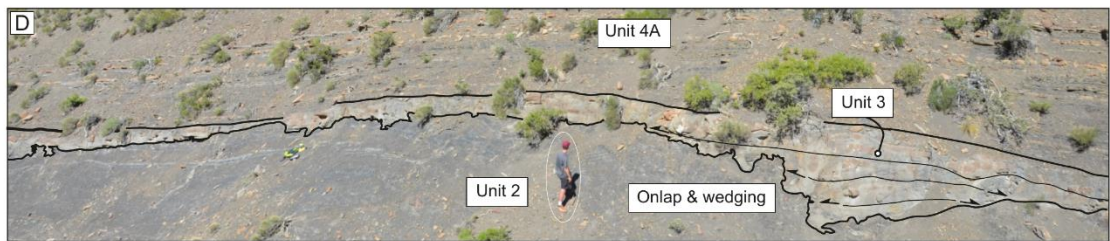
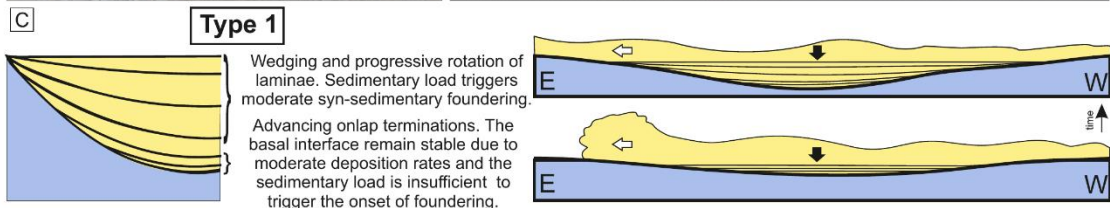
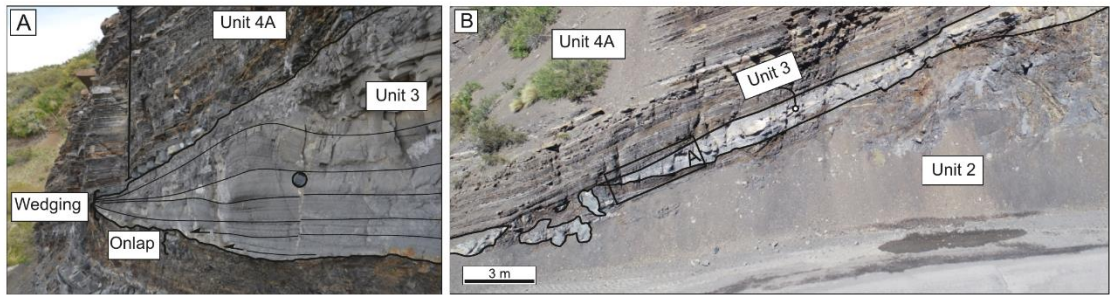


Fig. 8. Correlation panel focusing on the strata (Unit 3 and 4) overlying the debrisite (Unit 2). Note the colour bar next to each log representing the facies associations (see Fig. 5). Unit 3 is only present in western and eastern sectors whilst absent in the debrisite high (CML-12). The lower part of Unit 4A thins and onlaps the debrisite, while the upper one shows a larger lateral extent. Note the gravelly and tuff marker beds (red and white dashed lines, respectively). Unit 4A consists of an alternation between fine-grained lobe fringes and coarser healing lobe fringes in the western sector. Coarse-grained healing fringes pinch out, developing fine-grained lobe fringes in the eastern sector. Unit 4B consists of amalgamated thick-bedded sandstone of lobe axis, thinning into medium-bedded dominate lobe off-axis environment in the western sector. The sand-rich lobe thins and fines towards the east, pinching out in the central sector and interfingering with the lobe fringe deposits of Unit 4A. Note that the pinch-out terminations are developed where the debrisite relief is highest. The rose diagram shows the details of ripples (green), vergent convolute lamination (orange), Flame structures (yellow) and cross-bedding (red). Mean vectors of each type are shown, all suggesting a NE trend, except in Unit 4B, where the ripples suggest an E-directed palaeoflow indicating deflection processes. The perimeter of the rose diagrams corresponds to 100% of the value.



Key

Flow-direction ←

High-deposition rates ↓ ↓ ↓ ↓ ↓

Moderate-deposition rates ↓

Fig. 9. Illustrative diagram of foundered sandstone architecture and a model for their development.

Type 1: (A) Thin-bedded sandstone with onlap termination at the base, indicating interaction with inherited relief and wedging associated with the syn-depositional foundering. (B) Bodies wedge smoothly, forming lenticular bodies with flat tops. Note the location of A) indicated by a black rectangle. (C) Sketch of the architecture and evolutionary model of Type 1 architecture: Initial deposition is insufficient to trigger the foundering.

Type 2: (D) Thick-bedded foundered sandstones with associated thinner margins. Central parts are composed of sandstones deposited by high-density turbidity currents, whereas the thinner margins are sandstones interpreted as being deposited under more fluidal sediment gravity flows (Transitional flows). (E) Sketch of the architecture and evolutionary model of Type 2 architecture: Initial deposition is enough to trigger the foundering.

Type 3: (F) and (G) The shape of the thick-bedded sandstone bodies depends on the size and geometry of the thin-bedded megaclast. See Fig. 5 for more detail. (H) Sketch of the architecture and evolutionary model of Type 2 architecture: While foundering, the sandstone might be protruded by the megaclast due to its higher competence than the surrounding debrite matrix.

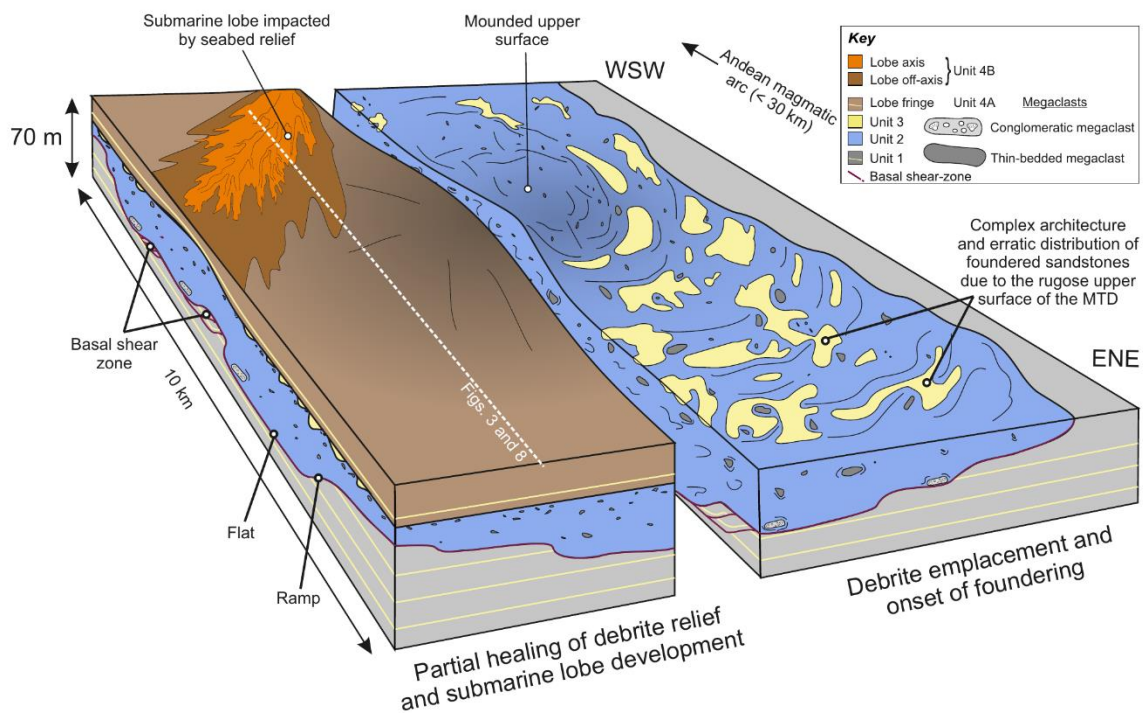


Fig. 10. Down-dip oriented schematic diagram illustrating the relief created by the debrite and the impact on younger sand-rich units. Foundered sandstones fill the small-scale rugosity,

leaving the kilometre-scale accommodation underfilled. The submarine gravity flows are deflected by long-lived subtle debrite-related relief (right block). Partial healing and drapping of the debrite with the progradation of submarine lobes, which are gently impacted by the long-lived inherited relief. Note the white dashed line representing the correlation shown in Fig. 3 and 8.

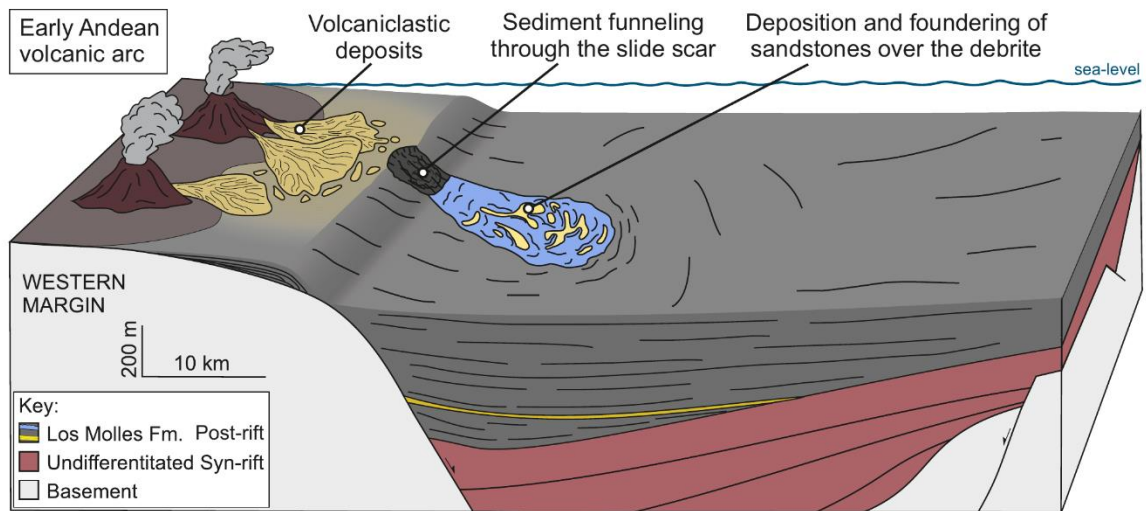


Fig. 11. Schematic diagram illustrating the role of the mass failure recorded in the Chacay Melehue depocenter as the trigger for downslope remobilisation of sand from shallow-marine settings.

REFERENCES

- Al Ja'Aidi, O.S., McCaffrey, W.D. and Kneller, B.C.** (2004) Factors influencing the deposit geometry of experimental turbidity currents: implications for sand-body architecture in confined basins. *Geol. Soc. London, Spec. Publ.*, **222**, 45–58.
- Allen, J.R.L.** (1971) Instantaneous sediment deposition rates deduced from climbing-ripple cross-lamination. *J. Geol. Soc. London.*, **127**, 553–561.
- Allen, J.R.L.** (1982) *Sedimentary structures, their character and physical basis* Volume 1. Elsevier. 663 pp.
- Alves, T.M.** (2015) Submarine slide blocks and associated soft-sediment deformation in deep-water basins: A review. *Mar. Pet. Geol.*, **67**, 262–285.
- Alves, T.M. and Cartwright, J.A.** (2009) Volume balance of a submarine landslide in the Espírito Santo Basin, offshore Brazil: Quantifying seafloor erosion, sediment accumulation and depletion. *Earth Planet. Sci. Lett.*, **288**, 572–580.
- Alves, T.M. and Lourenço, S.D.N.** (2010) Geomorphologic features related to gravitational collapse: Submarine landsliding to lateral spreading on a Late Miocene-Quaternary slope (SE Crete, eastern Mediterranean). *Geomorphology*, **123**, 13–33.
- Armitage, D.A., Romans, B.W., Covault, J.A. and Graham, S.A.** (2009) The Influence of Mass-Transport-Deposit Surface Topography on the Evolution of Turbidite Architecture: The Sierra Contreras, Tres Pasos Formation (Cretaceous), Southern Chile. *J. Sediment. Res.*, **79**, 287–301.
- Baas, J.H., Best, J.L. and Peakall, J.** (2016) Comparing the transitional behaviour of kaolinite and bentonite suspension flows. *Earth Surf. Process. Landforms*, **41**, 1911–1921.
- Baas, J.H., Best, J.L. and Peakall, J.** (2011) Depositional processes, bedform development and hybrid bed formation in rapidly decelerated cohesive (mud-sand) sediment flows. *Sedimentology*, **58**, 1953–1987.
- Baas, J.H., Best, J.L., Peakall, J. and Wang, M.** (2009) A Phase Diagram for Turbulent, Transitional, and Laminar Clay Suspension Flows. *J. Sediment. Res.*, **79**, 162–183.
- Baker, M.L., Baas, J.H., Malarkey, J., Jacinto, R.S., Craig, M.J., Kane, I.A. and Barker, S.** (2017) The effect of clay type on the properties of cohesive sediment gravity flows and their deposits. *J. Sediment. Res.*, **87**, 1176–1195.

- Bakke, K., Kane, I.A., Martinsen, O.J., Petersen, S.A., Johansen, T.A., Hustoft, S., Jacobsen, F.H. and Groth, A.** (2013) Seismic modeling in the analysis of deep-water sandstone termination styles. *Am. Assoc. Pet. Geol. Bull.*, **97**, 1395–1419.
- Blair, T.C. and McPherson, J.G.** (1999) Grain-size and textural classification of coarse sedimentary particles. *J. Sediment. Res.*, **69**, 6–19.
- Boulesteix, K., Poyatos-Moré, M., Hodgson, D.M., Flint, S.S. and Taylor, K.G.** (2020) Fringe or background: Characterizing deep-water mudstones beyond the basinfloor fan sandstone pinchout. *J. Sediment. Res.*, **90**, 1678–1705.
- Brooks, H.L., Hodgson, D.M., Brunt, R.L., Peakall, J. and Flint, S.S.** (2018) Exhumed lateral margins and increasing flow confinement of a submarine landslide complex. *Sedimentology*, **65**, 1067–1096.
- Browne, G.H., Bull, S., Arnot, M.J., Boyes, A.F., King, P.R. and Helle, K.** (2020) The role of mass transport deposits contributing to fluid escape: Neogene outcrop and seismic examples from north Taranaki, New Zealand. *Geo-Marine Lett.*, **40**, 789–807.
- Bull, S., Cartwright, J. and Huuse, M.** (2009) A review of kinematic indicators from mass-transport complexes using 3D seismic data. *Mar. Pet. Geol.*, **26**, 1132–1151.
- Butler, R.W.H., Eggenhuisen, J.T., Haughton, P. and McCaffrey, W.D.** (2016) Interpreting syndepositional sediment remobilization and deformation beneath submarine gravity flows; a kinematic boundary layer approach. *J. Geol. Soc. London.*, **173**, 46–58.
- Butler, R.W.H. and McCaffrey, W.D.** (2010) Structural evolution and sediment entrainment in mass-transport complexes: Outcrop studies from Italy. *J. Geol. Soc. London.*, **167**, 617–631.
- Cristallini, E., Bottesi, G., Gavarrino, A., Rodríguez, L., Tomezzoli, R. and Comeron, R.** (2006) Synrift geometry of the Neuquén Basin in northeastern Neuquén Province, Argentina. *Spec. Pap. Geol. Soc. Am.*, **407**, 147–161.
- Cumberpatch, Z.A., Soutter, E.L., Kane, I.A., Casson, M. and Vincent, S.J.** (2021) Evolution of a mixed siliciclastic-carbonate deep-marine system on an unstable margin: The Cretaceous of the Eastern Greater Caucasus, Azerbaijan. *Basin Res.*, **33**, 612–647.
- Dakin, N., Pickering, K.T., Mohrig, D. and Bayliss, N.J.** (2013) Channel-like features created by erosive submarine debris flows: Field evidence from the Middle Eocene Ainsa Basin, Spanish Pyrenees. *Mar. Pet. Geol.*, **41**, 62–71.

- Damborenea, S.E.** (1990) Middle Jurassic inoceramids from Argentina. *J. Paleontol.*, 736–759.
- Davis, C., Houghton, P., McCaffrey, W., Scott, E., Hogg, N. and Kitching, D.** (2009) Character and distribution of hybrid sediment gravity flow deposits from the outer Forties Fan, Palaeocene Central North Sea, UKCS. *Mar. Pet. Geol.*, **26**, 1919–1939.
- De La Cruz, R. and Suarez, M.** (1997) El Jurásico de la cuenca de Neuquén en lonquimay, Chile: formación nacientes del biobío (38-39°S). *Rev. Geol. Chile*, **24**, 3–24.
- Dykstra, M.** (2005) Dynamics of Submarine Sediment Mass-Transport, from the Shelf to the Deep Sea. *PhD Thesis*, 159.
- Dykstra, M., Garyfalou, K., Kertzus, V., Kneller, B.C., Milana, J.P., Molinaro, M., Szuman, M. and Thompson, P.** (2011) Mass-transport deposits: combining outcrop studies and seismic forward modeling to understand lithofacies distributions, deformation, and their seismic expression. In: *Posamentier, H., Weimer P. & Shipp, C. SEPM Special Publication 95*, 295–310.
- Eggenhuisen, J.T., Mccaffrey, W.D., Houghton, P.D.W. and Butler, R.W.H.** (2011) Shallow erosion beneath turbidity currents and its impact on the architectural development of turbidite sheet systems. *Sedimentology*, **58**, 936–959.
- Fairweather, L.** (2014) Mechanisms of supra MTD topography generation and the interaction of turbidity currents with such deposits. *PhD Thesis*, **1**, 242.
- Fallgatter, C., Kneller, B., Paim, P.S.G. and Milana, J.P.** (2017) Transformation, partitioning and flow–deposit interactions during the run-out of megafloes. *Sedimentology*, **64**, 359–387.
- Festa, A., Ogata, K., Pini, G.A., Dilek, Y. and Alonso, J.L.** (2016) Origin and significance of olistostromes in the evolution of orogenic belts: A global synthesis. *Gondwana Res.*, **39**, 180–203.
- Flores, G.** (1955) Les résultats des études pour les recherches pétrolifères en Sicile: Discussion. Proceedings of the 4th World Petroleum Congress. Casa Editrice Carlo Colombo. *Proc. 4th World Pet. Congr. Casa Ed. Carlo Colombo, Rome*, 121–122 (Section 1/A/2).
- Franzese, J., Spalletti, L., Gomez, I. and Macdonald, D.** (2003) Tectonic and paleoenvironmental evolution of Mesozoic sedimentary basins along the Andean foothills of Argentina (32 8 – 54 8 S). **16**, 81–90.
- Franzese, J.R. and Spalletti, L.A.** (2001) Late triassic- Early jurassic continental extension in SouthWestern Gondwana: Tectonic segmentation and pre-break-up rifting. *J. South Am. Earth*

Sci., **14**, 257–270.

Frey Martinez, J., Cartwright, J. and Hall, B. (2005) 3D seismic interpretation of slump complexes: Examples from the continental margin of Israel. *Basin Res.*, **17**, 83–108.

Fugelli, E. M., Olsen, T.R. (2007) Delineating confined slope turbidite systems offshore mid-Norway: The Cretaceous deep-marine Lysing Formation. *Am. Assoc. Pet. Geol. Bull.*, **91**, 1577–1601.

Gee, M.J.R., Gawthorpe, R.L. and Friedmann, S.J. (2006) Triggering and Evolution of a Giant Submarine Landslide, Offshore Angola, Revealed by 3D Seismic Stratigraphy and Geomorphology. *J. Sediment. Res.*, **76**, 9–19.

Gulisano, C. and Gutiérrez Pleimling, A.R. (1995) Field Guide. The Jurassic of the Neuquén Basin. a) Neuquén Province: Asociación Geológica Argentina. *Série E*, **2**, 1–111.

Gulisano, C.A., Gutiérrez Pleimling, A.R. and Digregorio, J.H. (1984) Esquema estratigráfico de la secuencia jurásica del oeste de la provincia del Neuquén. IX Congr. Geológico Argentino 1:236–259.

Hampton, M.A., Lee, H.J. and Locat, J. (1995) Submarine Landslides. *Rev. Geophys.*, **34**, 33-59.

Hansen, L.A.S., Hodgson, D.M., Pontén, A., Bell, D. and Flint, S. (2019) Quantification of basin-floor fan pinchouts: Examples from the Karoo Basin, South Africa. *Front. Earth Sci.*, **7**, 1–20.

Hansen, L.A.S., Hodgson, D.M., Pontén, A., Thrana, C. and Obradors Latre, A. (2021) Mixed axial and transverse deep-water systems: The Cretaceous post-rift Lysing Formation, offshore Norway. *Basin Res.*, 1–23.

Haughton, P., Davis, C., McCaffrey, W. and Barker, S. (2009) Hybrid sediment gravity flow deposits - Classification, origin and significance. *Mar. Pet. Geol.*, **26**, 1900–1918.

Haughton, P.D.W., Barker, S.P. and McCaffrey, W.D. (2003) “Linked” debrites in sand-rich turbidite systems - Origin and significance. *Sedimentology*, **50**, 459–482.

Hodgson, D.M. (2009) Distribution and origin of hybrid beds in sand-rich submarine fans of the Tanqua depocentre, Karoo Basin, South Africa. *Mar. Pet. Geol.*, **26**, 1940–1956.

Hodgson, D.M., Brooks, H.L., Ortiz-Karpf, A., Spychala, Y., Lee, D.R. and Jackson, C.A.-L. (2019) Entrainment and abrasion of megaclasts during submarine landsliding and their impact on flow behaviour. *Geol. Soc. London, Spec. Publ.*, **477**, 223–240.

- Howell, J.A., Swcharz, E., Spalletti, L.A. and Veiga, G.D.** (2005) The Neuquén Basin, Argentina: A case study in sequence stratigraphy and basin dynamics. *Geol. Soc. London, Spec. Publ.*, **252**, 1–14.
- Iverson, R.M.** (1997) The physics of debris flows. *Rev. Geophys.*, **35**, 245–296.
- Jackson, C.A.L.** (2011) Three-dimensional seismic analysis of megaclast deformation within a mass transport deposit; Implications for debris flow kinematics. *Geology*, **39**, 203–206.
- Jackson, C.A.L. and Johnson, H.D.** (2009) Sustained turbidity currents and their interaction with debrite-related topography; Labuan Island, offshore NW Borneo, Malaysia. *Sediment. Geol.*, **219**, 77–96.
- Jobe, Z.R., Lowe, D.R. and Morris, W.R.** (2012) Climbing-ripple successions in turbidite systems : depositional environments , sedimentation rates and accumulation times. 867–898.
- Kamo, S.L. and Riccardi, A.C.** (2009) A new U-Pb zircon age for an ash layer at the Bathonian-Callovian boundary, Argentina. *Gff*, **131**, 177–182.
- Kane, I.A. and Pontén, A.S.M.** (2012) Submarine transitional flow deposits in the Paleogene Gulf of Mexico. *Geology*, **40**, 1119–1122.
- Kane, I.A., Pontén, A.S.M., Vangdal, B., Eggenhuisen, J.T., Hodgson, D.M. and Spychala, Y.T.** (2017) The stratigraphic record and processes of turbidity current transformation across deep-marine lobes. *Sedimentology*, **64**, 1236–1273.
- Kleverlaan, K.** (1987) Gordo megabed: a possible seismite in a tortonian submarine fan, tabernas basin, province almeria, southeast spain. *Sediment. Geol.*, **51**, 165–180.
- Kneller, B., Dykstra, M., Fairweather, L. and Milana, J.P.** (2016) Mass-transport and slope accommodation: implications for turbidite sandstone reservoirs. *Am. Assoc. Pet. Geol. Bull.*, **100**, 213–235.
- Kneller, B.C. and Branney, M.J.** (1995) Sustained high-density turbidity currents and the deposition of thick massive sands. *Sedimentology*, **42**, 607–616.
- Könitzer, S.F., Davies, S.J., Stephenson, M.H. and Leng, M.J.** (2014) Depositional controls on mudstone lithofacies in a basinal setting: Implications for the delivery of sedimentary organic matter. *J. Sediment. Res.*, **84**, 198–214.
- Labauve, P., Mutti, E. and Seguret, M.** (1987) Megaturbidites : A Depositional Model From the Eocene. *Geo-Marine Lett.*, **7**, 91–101.

- Leanza, H.A., Mazzini, A., Corfu, F., Llambías, E.J., Svensen, H., Planke, S. and Galland, O.** (2013) The Chachil Limestone (Pliensbachian-earliest Toarcian) Neuquén Basin, Argentina: U-Pb age calibration and its significance on the Early Jurassic evolution of southwestern Gondwana. *J. South Am. Earth Sci.*, **42**, 171–185.
- Lee, C., Nott, J.A., Keller, F.B. and Parrish, A.R.** (2004) Seismic expression of the cenozoic mass transport complexes deepwater Tarfaya-Agadir Basin offshore Morocco. *Proc. Annu. Offshore Technol. Conf.*, **3**, 1891–1908.
- Legarreta, L.** (1991) Evolution of a Callovian-Oxfordian carbonate margin in the Neuquén Basin of west-central Argentina: facies, architecture, depositional sequences and global sea-level changes. *Sediment Geol.* doi: 10.1016/0037-0738(91)90142-Z
- Legarreta, L. and Gulisano, C.A.** (1989) Análisis estratigráfico secuencial de la Cuenca Neuquina (Triásico superior-Terciario inferior). In: *Cuencas sedimentarias argentinas.*, 221–243.
- Legarreta, L. and Uliana, M.A.** (1996) The Jurassic succession in west-central Argentina: Stratal patterns, sequences and paleogeographic evolution. *Palaeogeogr. Palaeoclimatol. Palaeoecol.*, **120**, 303–330.
- Legros, F.** (2002) Can dispersive pressure cause inverse grading in grain flows? *J. Sediment. Res.*, **72**, 166–170.
- Lien, T.** (2005) From rifting to drifting: Effects on the development of deep-water hydrocarbon reservoirs in a passive margin setting, Norwegian Sea.
- Llambías, E.J. and Leanza, H.A.** (2005) Depósitos laháricos en la formación los molles en chacay mehue, neuquén: Evidencia de volcanismo jurásico en la cuenca neuquina. *Rev. la Asoc. Geol. Argentina*, **60**, 552–558.
- Llambías, E.J., Leanza, H.A. and Carbone, O.** (2007) Evolución Tectono-magmática durante el pérmico al Jurásico temprano en la Cordillera del Viento (37°05'S - 37°15'S): Nuevas evidencias geológicas y geoquímicas Del Inicio de la Cuencas Neuquina. *Rev. la Asoc. Geol. Argentina*, **62**, 217–235.
- Llambías, E.J., Quenardelle, S. and Montenegro, T.** (2003) The Choiyoi Group from central Argentina: A subalkaline transitionalto alkaline association in the craton adjacent to the active marginof the Gondwana continent. *J. South Am. Earth Sci.*, **16**, 243–257.
- Lowe, D.R.** (1982) Sediment gravity flows; II, Depositional models with special reference to the deposits of high-density turbidity currents. *J. Sediment. Res.*, **52**, 279-297.

- Lowe, D.R. and Guy, M.** (2000) Slurry-flow deposits in the Britannia Formation (Lower Cretaceous), North Sea: A new perspective on the turbidity current and debris flow problem. *Sedimentology*, **47**, 31–70.
- Lucente, C.C. and Pini, G.A.** (2003) Anatomy and emplacement mechanism of a large submarine slide within a miocene foredeep in the Northern Apennines, Italy: A field perspective. *Am. J. Sci.*, **303**, 565–602.
- Major, J.J. and Iverson, R.M.** (1999) Debris-flow deposition: Effects of pore-fluid pressure and friction concentrated at flow margins. *Bull. Geol. Soc. Am.*, **111**, 1424–1434.
- Maceda, R. and Figueroa, D.** (1995) Inversion of the Mesozoic Neuquen Rift in the Malargue fold and thrust belt, Mendoza, Argentina. *Pet. basins South Am.*, **62**, 369–382.
- McClelland, H.L.O., Woodcock, N.H. and Gladstone, C.** (2011) Eye and sheath folds in turbidite convolute lamination: Aberystwyth Grits Group, Wales. *J. Struct. Geol.*, **33**, 1140–1147.
- McGilvery, T.A. and Cook, D.L.** (2003) The Influence of Local Gradients on Accommodation Space and Linked Depositional Elements Across a Stepped Slope Profile, Offshore Brunei. Shelf Margin Deltas Linked Down Slope Pet. Syst. 23rd Annu. 387–419.
- Migeon, S., Ceramicola, S., Praeg, D., Ducassou, E., Dano, A., Ketzer, J.M., Mary, F. and Mascle, J.** (2014) Post-failure Processes on the Continental Slope of the Central Nile Deep-Sea Fan: Interactions Between Fluid Seepage, Sediment Deformation and Sediment-Wave Construction. In: *Submarine Mass Movements and Their Consequences. Advances in Natural and Technological Hazards Research, vol 37*. Springer, Cham. https://doi.org/10.1007/978-3-319-00972-8_11, 201–212.
- Moscardelli, L. and Wood, L.** (2008) New classification system for mass transport complexes in offshoreTrinidad. 73–98.
- Moscardelli, L., Wood, L. and Mann, P.** (2006) Mass-transport complexes and associated processes in the offshore area of Trinidad and Venezuela. *Am. Assoc. Pet. Geol. Bull.*, **90**, 1059–1088.
- Mulder, T. and Alexander, J.** (2001) The physical character of subaqueous sedimentary density flows and their deposits. *Sedimentology*, **48**, 269–299.
- Mutti, E.** (1977) Distinctive thin-bedded turbidite facies and related depositional environments in the Eocene Hecho Group (South-central Pyrenees, Spain). *Sedimentology*, **24**, 107–131.

- Nardin, T.R., Hein, F.J., Gorsline, D.S. and Edwards, B.D.** (1979) A review of mass movement processes sediment and acoustic characteristics, and contrasts in slope and base-of-slope systems versus canyon-fan-basin floor systems. *SEPM Spec. Publ.*, **27**, 61–73.
- Nugraha, H.D., Jackson, C.A.L., Johnson, H.D., Hodgson, D.M. and Clare, M.** How erosive are submarine landslides?
- Nwoko, J., Kane, I. and Huuse, M.** (2020a) Megaclasts within mass-transport deposits: Their origin, characteristics and effect on substrates and succeeding flows. *Geol. Soc. Spec. Publ.*, **500**, 515–530.
- Nwoko, J., Kane, I. and Huuse, M.** (2020b) Mass transport deposit (MTD) relief as a control on post-MTD sedimentation: Insights from the Taranaki Basin, offshore New Zealand. *Mar. Pet. Geol.*, **120**, 104489.
- Ogata, K., Festa, A., Pini, G.A. and Alonso, J.L.** (2019) Submarine landslide deposits in orogenic belts: olistostromes and sedimentary mélanges. In: *Submarine Landslides: Subaqueous Mass Transport Deposits from Outcrops to Seismic Profiles*, 1–26.
- Ogata, K., Mountjoy, J.J., Pini, G.A., Festa, A. and Tinterri, R.** (2014a) Shear zone liquefaction in mass transport deposit emplacement: A multi-scale integration of seismic reflection and outcrop data. *Mar. Geol.*, **356**, 50–64.
- Ogata, K., Mutti, E., Pini, G.A. and Tinterri, R.** (2012) Mass transport-related stratal disruption within sedimentary mélanges: Examples from the northern Apennines (Italy) and south-central Pyrenees (Spain). *Tectonophysics*, **568–569**, 185–199.
- Ogata, K., Pogačnik, Z., Pini, G.A., Tunis, G., Festa, A., Camerlenghi, A. and Rebesco, M.** (2014b) The carbonate mass transport deposits of the Paleogene Friuli Basin (Italy/Slovenia): Internal anatomy and inferred genetic processes. *Mar. Geol.*, **356**, 88–110.
- Ortiz-Karpf, A., Hodgson, D.M., Jackson, C.A.-L. and McCaffrey, W.D.** (2017) Influence of Seabed Morphology and Substrate Composition On Mass-Transport Flow Processes and Pathways: Insights From the Magdalena Fan, Offshore Colombia. *J. Sediment. Res.*, **87**, 189–209.
- Ortiz-Karpf, A., Hodgson, D.M. and McCaffrey, W.D.** (2015) The role of mass-transport complexes in controlling channel avulsion and the subsequent sediment dispersal patterns on an active margin: The Magdalena Fan, offshore Colombia. *Mar. Pet. Geol.*, **64**, 58–75.
- Owen, G.** (1987) Deformation processes in unconsolidated sands. *Geol. Soc. Spec. Publ.*, **29**, 11–24.

- Owen, G.** (2003) Load structures: Gravity-driven sediment mobilization in the shallow subsurface. *Geol. Soc. Spec. Publ.*, **216**, 21–34.
- Pángaro, F., Pereira, D.M. and Micucci, E.** (2009) El sinrift de la dorsal de Huincul, Cuenca Neuquina: Evolución y control sobre la estratigrafía y estructura del área. *Rev. la Asoc. Geol. Argentina*, **65**, 265–277.
- Payros, A. and Pujalte, V.** (2019) Eocene Mass-Transport Deposits in the Basque Basin (Western Pyrenees, Spain). 155–170.
- Payros, A., Pujalte, V. and Orue-Etxebarria, X.** (1999) The South Pyrenean Eocene carbonate megabreccias revisited: New interpretation based on evidence from the Pamplona Basin. *Sediment. Geol.*, **125**, 165–194.
- Pickering, K.T. and Corregidor, J.** (2005) Mass-transport complexes (MTCs) and tectonic control on basin-floor submarine fans, middle Eocene, South Spanish Pyrenees. *J. Sediment. Res.*, **75**, 761–783.
- Praeg, D., Ketzer, J.M., Adolpho Herbert, A., Migeon, S., Ceramicola, S., Alexandre, D., Emmanuelle, Ducassou Stéphanie, D., Jean, M. and Rodrigues, L.F.** (2014) Fluid seepage in relation to seabed deformation on the central Nile deep-sea fan, part 2: evidence from multibeam and sidescan imagery. In: *Submarine Mass Movements and Their Consequences. Advances in Natural and Technological Hazards Research. 6th International Symposium. Volume 37*. https://doi.org/10.1007/978-3-319-00972-8_11, 37, 141–150.
- Prélat, A., Hodgson, D.M. and Flint, S.S.** (2009) Evolution, architecture and hierarchy of distributary deep-water deposits: a high-resolution outcrop investigation from the Permian Karoo Basin, South Africa. *Sedimentology*, **56**, 2132–2154.
- Privat, A.M.J., Hodgson, D.M., Jackson, C.A., Schwarz, E. and Peakall, J.** (2021) Evolution from syn-rift carbonates to early post-rift deep-marine intraslope lobes: The role of rift basin physiography on sedimentation patterns. *Sedimentology*, 0–2.
- Riccardi, A. and Kamo, S.** (2014) Biostratigraphy and Geochronology of the Pliensbachian-Toarcian Boundary in Argentina. *XIX Congr. Geológico Argentino, Junio 2014, Córdoba, Actas T1-4*, 9–11.
- Riccardi, A.C.** (2008) The marine Jurassic of Argentina: A biostratigraphic framework. *Episodes*, **31**, 326–335.
- Riccardi, A.C., Damborenea, S.E., Manceñido, M.O. and Leanza, H.A.** (2011) Megainvertebrados del

- Jurásico y su importancia geobiológica. *Relat. del XVIII Congr. Geológico Argentino, Neuquén*, 441–464.
- Rosenfeld, U. and Volldaeimer, W.** (1980) Turbidite und andere Rhythmite im tieferen Jura des Neuquén-Beckens (Argentinien). 379–421.
- Sawyer, D.E., Flemings, P.B., Dugan, B. and Germaine, J.T.** (2009) Retrogressive failures recorded in mass transport deposits in the Ursa Basin, Northern Gulf of Mexico. *J. Geophys. Res. Solid Earth*, **114**, 1–20.
- Sinclair, H.D. and Tomasso, M.** (2002) Depositional Evolution of Confined Turbidite Basins. *J. Sediment. Res.*, **72**, 451–456.
- Sobiesiak, M.S., Kneller, B., Alsop, G.I. and Milana, J.P.** (2016) Internal deformation and kinematic indicators within a tripartite mass transport deposit, NW Argentina. *Sediment. Geol.*, **344**, 364–381.
- Southern, S.J., Patacci, M., Felletti, F. and McCaffrey, W.D.** (2015) Influence of flow containment and substrate entrainment upon sandy hybrid event beds containing a co-genetic mud-clast-rich division. *Sediment. Geol.*, **321**, 105–122.
- Soutter, E.L., Kane, I.A., Fuhrmann, A., Cumberpatch, Z.A. and Huuse, M.** (2019) The stratigraphic evolution of onlap in siliciclastic deep-water systems: Autogenic modulation of allogenic signals. *J. Sediment. Res.*, **89**, 890–917.
- Soutter, E.L., Kane, I.A. and Huuse, M.** (2018) Giant submarine landslide triggered by Paleocene mantle plume activity in the North Atlantic. *Geology*, **46**, 511–514.
- Spalletti, L.A., Parent, H., Veiga, G.D. and Schwarz, E.** (2012) Amonites y bioestratigrafía del Grupo Cuyo en la Sierra de Reyes (cuenca Neuquina central, Argentina) y su significado secuencial. *Andean Geol.*, **39**, 464–481.
- Spychala, Y.T., Hodgson, D.M., Prélat, A., Kane, I.A., Flint, S.S. and Mountney, N.P.** (2017a) Frontal and lateral submarine lobe fringes: Comparing sedimentary facies, architecture and flow processes. *J. Sediment. Res.*, **87**, 75–96.
- Spychala, Y.T., Hodgson, D.M., Stevenson, C.J. and Flint, S.S.** (2017b) Aggradational lobe fringes: The influence of subtle intrabasinal seabed topography on sediment gravity flow processes and lobe stacking patterns. *Sedimentology*, **64**, 582–608.

- Stevenson, C.J., Jackson, C.A., Hodgson, D.M., Hubbard, S.M. and Eggenhuisen, J.T.** (2015) Deep-water sediment bypass. 1058–1081.
- Stevenson, C.J., Peakall, J., Hodgson, D.M., Bell, D. and Privat, A.** (2020) TB OR NOT TB: BANDING IN TURBIDITE SANDSTONES. *J. Sediment. Res.*, **90**, 821–842.
- Steventon, M.J., Jackson, C.A., Johnson, H.D. and Hodgson, D.M.** (2021) Evolution of a sand-rich submarine channel-lobe system, and the impact of mass-transport and transitional-flow deposits on reservoir heterogeneity: Magnus Field, Northern North Sea.
- Steventon, M.J., Jackson, C.A.L., Hodgson, D.M. and Johnson, H.D.** (2020) Lateral variability of shelf-edge and basin-floor deposits, Santos Basin, Offshore Brazil. *J. Sediment. Res.*, **90**, 1198–1221.
- Stow, D.A.V. and Johansson, M.** (2000) Deep-water massive sands: Nature, origin and hydrocarbon implications. *Mar. Pet. Geol.*, **17**, 145–174.
- Suárez, M. and de la Cruz, R.** (1997) Volcanismo pliniano del Lías durante los inicios de la cuenca de Neuquén, Cordillera del Viento, Neuquén, Argentina. *Actas 7º Congr. Geológico Chil.* 266–270.
- Sumner, E.J., Amy, L.A. and Talling, P.J.** (2008) Deposit structure and processes of sand deposition from decelerating sediment suspensions. *J. Sediment. Res.*, **78**, 529–547.
- Talling, P.J., Amy, L.A. and Wynn, R.B.** (2007) New insight into the evolution of large-volume turbidity currents: Comparison of turbidite shape and previous modelling results. *Sedimentology*, **54**, 737–769.
- Talling, P.J., Masson, D.G., Sumner, E.J. and Malgesini, G.** (2012) Subaqueous sediment density flows: Depositional processes and deposit types. *Sedimentology*, **59**, 1937–2003.
- Tinterri, R.** (2011) Combined flow sedimentary structures and the genetic link between sigmoidal-and hummocky-cross stratification.
- Tinterri, R., Muzzi Magalhaes, P., Tagliaferri, A. and Cunha, R.S.** (2016) Convolute laminations and load structures in turbidites as indicators of flow reflections and decelerations against bounding slopes. Examples from the Marnoso-arenacea Formation (northern Italy) and Annot Sandstones (south eastern France). *Sediment. Geol.*, **344**, 382–407.
- Trabucho-Alexandre, J., Dirkx, R., Veld, H., Klaver, G. and De Boer, P.L.** (2012) Toarcian black shales in the dutch central graben: Record of energetic, variable depositional conditions during an oceanic anoxic event. *J. Sediment. Res.*, **82**, 104–120.

- Twiss, R.J. and Moores, E.M.** (1992) Structural Geology. W.H. Freeman and Company, New York.
- Valdez, V., Milana, J.P., Sobiesiak, M.S. and Kneller, B.** (2019) The Carboniferous MTD Complex at La Peña Canyon, Paganzo Basin (San Juan, Argentina). In: *Submarine Landslides: Subaqueous Mass Transport Deposits from Outcrops to Seismic Profiles*, 105–116.
- Van der Merwe, W.C., Hodgson, D.M. and Flint, S.S.** (2009) Widespread syn-sedimentary deformation on a muddy deep-water basin-floor: The vischkuil formation (Permian), Karoo Basin, South Africa. *Basin Res.*, **21**, 389–406.
- Van Der Merwe, W.C., Hodgson, D.M. and Flint, S.S.** (2011) Origin and terminal architecture of a submarine slide: A case study from the Permian Vischkuil Formation, Karoo Basin, South Africa. *Sedimentology*, **58**, 2012–2038.
- Veiga, G.D., Schwarz, E. and Spalletti, L.A.** (2011) Análisis estratigráfico de la Formación Lotena (Calloviano superior- Oxfordiano inferior) en la Cuenca Neuquina Central, República Argentina. Integración de información de afloramientos y subsuelo. *Andean Geol.*, **38**, 171–197.
- Veiga, G.D., Schwarz, E., Spalletti, L.A. and Massafiero, J.L.** (2013) Anatomy And Sequence Architecture of the Early Post-Rift In the Neuquen Basin (Argentina): A Response To Physiography and Relative Sea-Level Changes. *J. Sediment. Res.*, **83**, 746–765.
- Vergani, G.D., Tankard, A.J., Belotti, H.J. and Welsink, H.J.** (1995) Tectonic Evolution and Paleogeography of the Neuquén Basin, Argentina. *Pet. basins South Am.*, **1904**, 383–402.
- Vicente, J.C.** (2005) Dynamic paleogeography of the Jurassic Andean Basin: Pattern of transgression and localisation of main straits through the magmatic arc. *Rev. la Asoc. Geol. Argentina*, **60**, 221–250.
- Watt, S.F.L., Talling, P.J., Vardy, M.E., Masson, D.G., Henstock, T.J., Hühnerbach, V., Minshull, T.A., Urlaub, M., Lebas, E., Le Friant, A., Berndt, C., Crutchley, G.J. and Karstens, J.** (2012) Widespread and progressive seafloor-sediment failure following volcanic debris avalanche emplacement: Landslide dynamics and timing offshore Montserrat, Lesser Antilles. *Mar. Geol.*, **323–325**, 69–94.
- Weaver, C.** (1931) Paleontology of the Jurassic and Cretaceous of West Central Argentina. Memoir University of Washington 1.
- Weaver, C.** (1942) A general summary of the Mesozoic of South and Central America. In: *Proceedings of the eighth American scientific congress held in Washington May 10-18*, 149–193.

Zöllner, W. and Amos, A.J. (1973) Descripción geológica de la hoja 32b, Chos Malal. Servicio Geológico Nacional. 97 pp.